CM² MAGAZINE

第 80 期

南方科技大学海洋磁学中心主编

http://cm2.sustech.edu.cn/

创刊词

海洋是生命的摇篮，是文明的纽带。地球上最早的生命诞生于海洋，海洋里的生命最终进化成了人类，人类的文化融合又通过海洋得以实现。人因海而兴。

人类对海洋的探索从未停止。从远古时代美丽的神话传说，到麦哲伦的全球航行，再到现代对大洋的科学钻探计划，海洋逐渐从人类敬畏崇拜幻想的精神寄托演变成可以开发利用与科学研究的客观存在。其中，上个世纪与太空探索同步发展的大洋科学钻探计划将人类对海洋的认知推向了崭新的纬度：深海（deep sea）与深时（deep time）。大洋钻探计划让人类知道，奔流不息的大海之下，埋藏的却是亿万年的地球历史。它们记录了地球板块的运动，从而使板块构造学说得到证实；它们记录了地球环境的演变，从而让古海洋学方兴未艾。

在探索海洋的悠久历史中，从大航海时代的导航，到大洋钻探计划中不可或缺的磁性地层学，磁学发挥了不可替代的作用。这不是偶然，因为从微观到宏观，磁性是最基本的物理属性之一，可以说，万物皆有磁性。基于课题组的学科背景和对海洋的理解，我们对海洋的探索以磁学为主要手段，海洋磁学中心因此而生。

海洋磁学中心，简称 CM^2，一为其全名“Centre for Marine Magnetism”的缩写，另者恰与爱因斯坦著名的质能方程 $E = MC^2$ 对称，借以表达我们对科学巨匠的敬仰和对科学的不懈追求。

然而科学从来不是单打独斗的产物。我们以磁学为研究海洋的主攻利器，但绝不仅限于磁学。凡与磁学相关的领域均是我们关注的重点。为了跟踪反映国内外地球科学特别是与磁学有关的地球科学领域的最新研究进展，海洋磁学中心特地主办 CM^2 Magazine，以期与各位地球科学工作者相互交流学习、合作共进！

“海洋孕育了生命，联通了世界，促进了发展”。 21 世纪是海洋科学的时代，由陆向海，让我们携手迈进中国海洋科学的黄金时代。

目录

1. 地震双重体揭示湖相地震—浊积岩中多次脉冲式作用

翻译人：仲义 zhongy@sustech.edu.cn

Katleen W, Maxim D, Catherine K, et al. ***Earthquake doublet revealed by multiple pulses in lacustrine seismo-turbidites****[J] Geology, online.*

https://doi.org/10.1130/G48940.1

摘要：在世界各地的断层系统中都有描述过地震双重现象，但在古地震中还没有得到确切的解释。我们目前的认识仅限于历史事件，阻止了研究人员发现潜在的模式或识别常见的断层行为。因此，识别出古记录中双重体特征对于地震灾害评估和降低风险至关重要。作者基于多脉冲式浊流的流向分析，提出了一种新型方法来揭示湖相古地震记录中的地震双重体特征。因为来自同一震源位置的浊流延迟出现表明个别触发机制的发生。由于颗粒在水流中存在定向排列，作者结核颗粒尺寸、古地磁学和高分辨率 X 射线断层扫描的方法来确定细长颗粒的主轴方向，从而分析水流的动力方向。该方法被应用于 2007 年西苏门答腊地震中（震级 6.4 - 6.3 级，间隔 2 小时）产生的沉积浊积岩，它提供了一个明确无误的地震双重层沉积证据。作者认为，该方法对各种水下古地震记录的多脉冲浊流有很大的应用潜力，可以揭示未来地震序列的发生。

ABSTRACT: Earthquake doublets have been described in fault systems around the world but have not yet been confidently resolved in paleoseismic records. Our current knowledge is limited to historical occurrences, preventing researchers from uncovering potential patterns or recognizing common fault behavior. Identification of prehistoric doublets is thus of crucial importance for adequate seismic hazard assessment and risk mitigation. We developed a new methodology to reveal the sedimentary imprint of earthquake doublets in lacustrine paleoseismic records based on flow direction analysis in multipulsed turbidites, because the delayed arrival of turbidity currents originating from the same source location demonstrates the occurrence of individual triggering mechanisms. As grains tend to align in the presence of a flow, we analyzed flow

directions by determining the dominant orientation of elongated grains using a combination of grain size, paleomagnetism, and high-resolution X-ray computed tomography. This methodology was applied to a turbidite deposited by the 2007 CE earthquakes in West Sumatra (Mw 6.4 and 6.3, 2 h apart), and it provides the first unmistakable sedimentary evidence for an earthquake doublet. We argue that this methodology has great potential to be applied to multipulsed turbidites in various subaquatic paleoseismic records and can reveal the occurrence of unknown earthquake sequences.

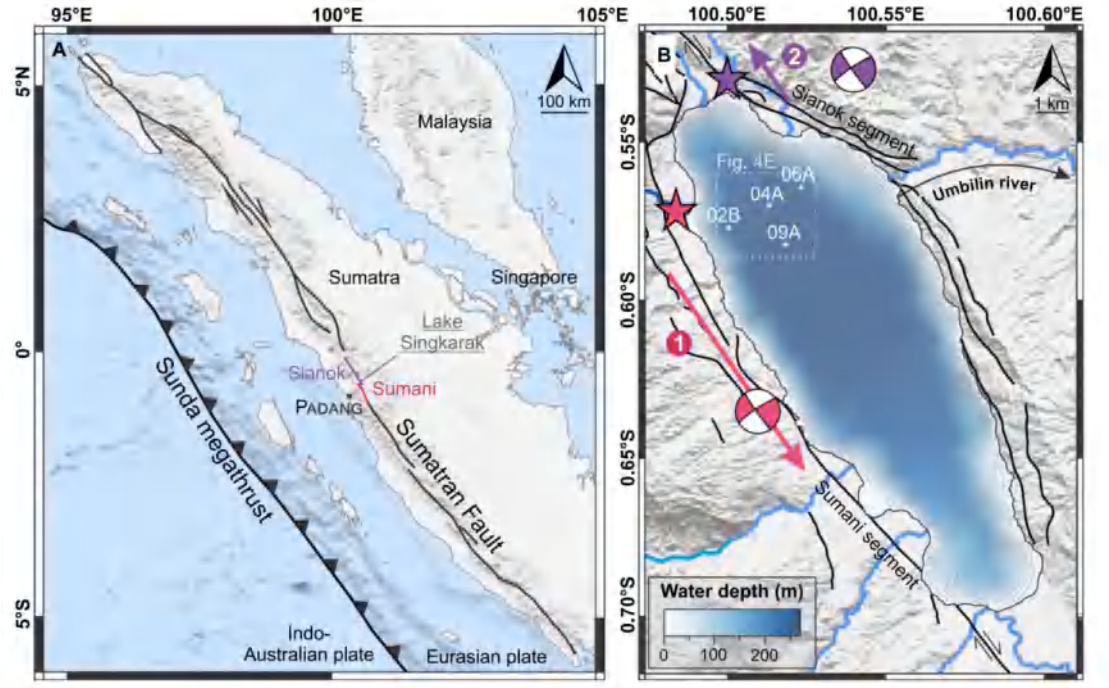

Figure 1. (A) Setting of Lake Singkarak, West Sumatra, located on the Sumani and Sianok segments of the Sumatran fault and along the Sunda megathrust. The lake is located close to the regional capital of Padang. (B) Bathymetric map of the lake (20 m contours) showing locations of four studied cores (SN17–02B, SN17–04A, SN17–06A, and SN17–09A) and the most important rivers. Fault traces of both segments involved in the 2007 CE earthquake doublet are after Sieh and Natawidjaja (2000); rupture propagation (colored arrows), epicenter locations, and focal mechanisms are after Nakano et al. (2010). Figure is modified from Wils et al. (2021).

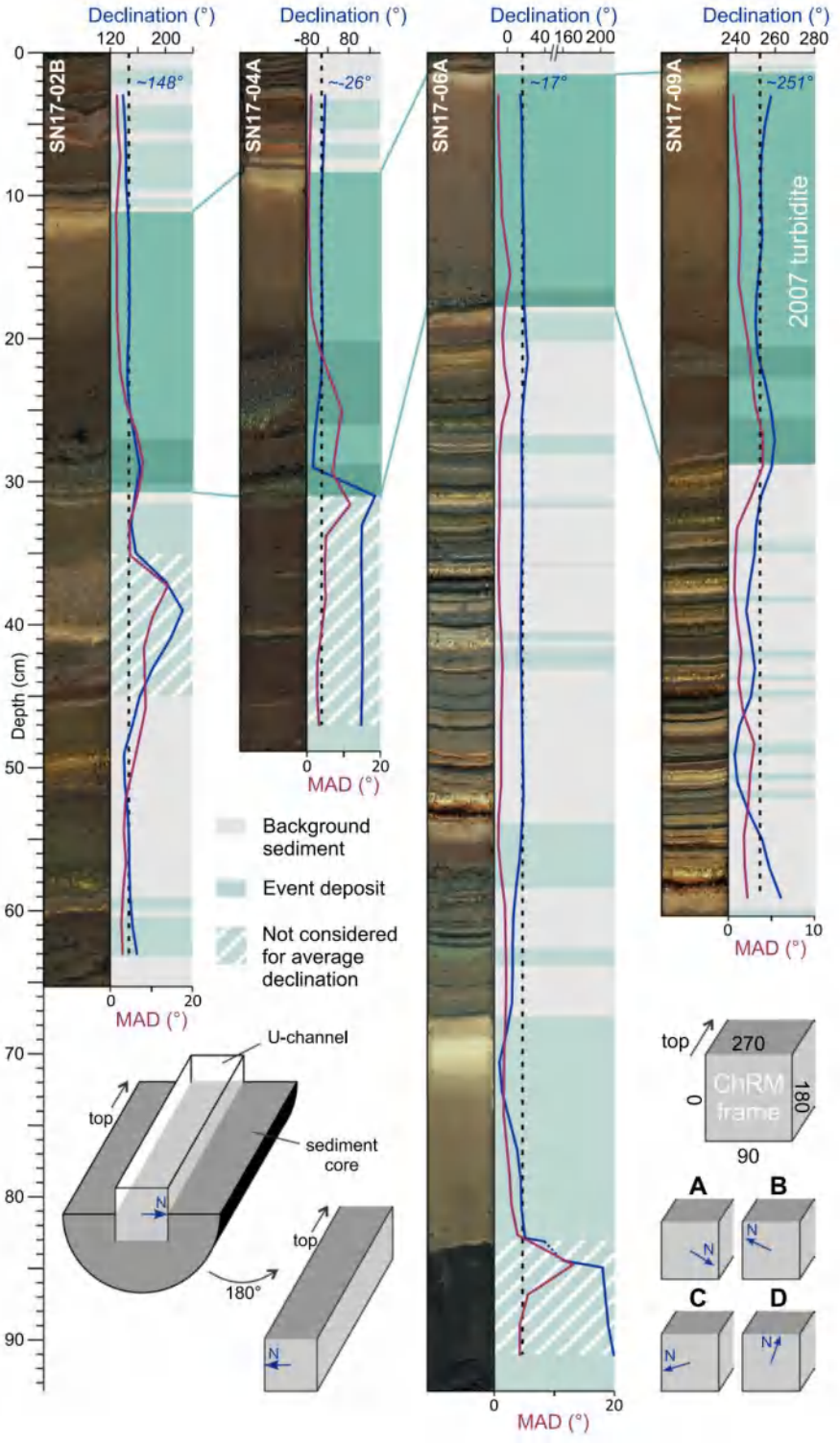

Figure 2. Declination (dark blue) and maximum angular deviation (MAD, purple) derived from paleomagnetic analysis of four cores from Lake Singkarak (West Sumatra), with interpretation of background (gray) and event sedimentation (green) following Wils et al. (2021). Here, the 2007 CE seismo-turbidite and its coarse-grained intervals are indicated in dark green (see Fig. 3). Average declination (dashed line) indicates north direction in characteristic remanent magnetization (ChRM)

reference frame for each U-channel, calculated by discarding event deposits with unreliable declination values (white shading). Lower-left schematic shows a representation of the U-channel with respect to the sediment core. Lower-right schematic shows U-channel bottom views that show declination direction for each core.

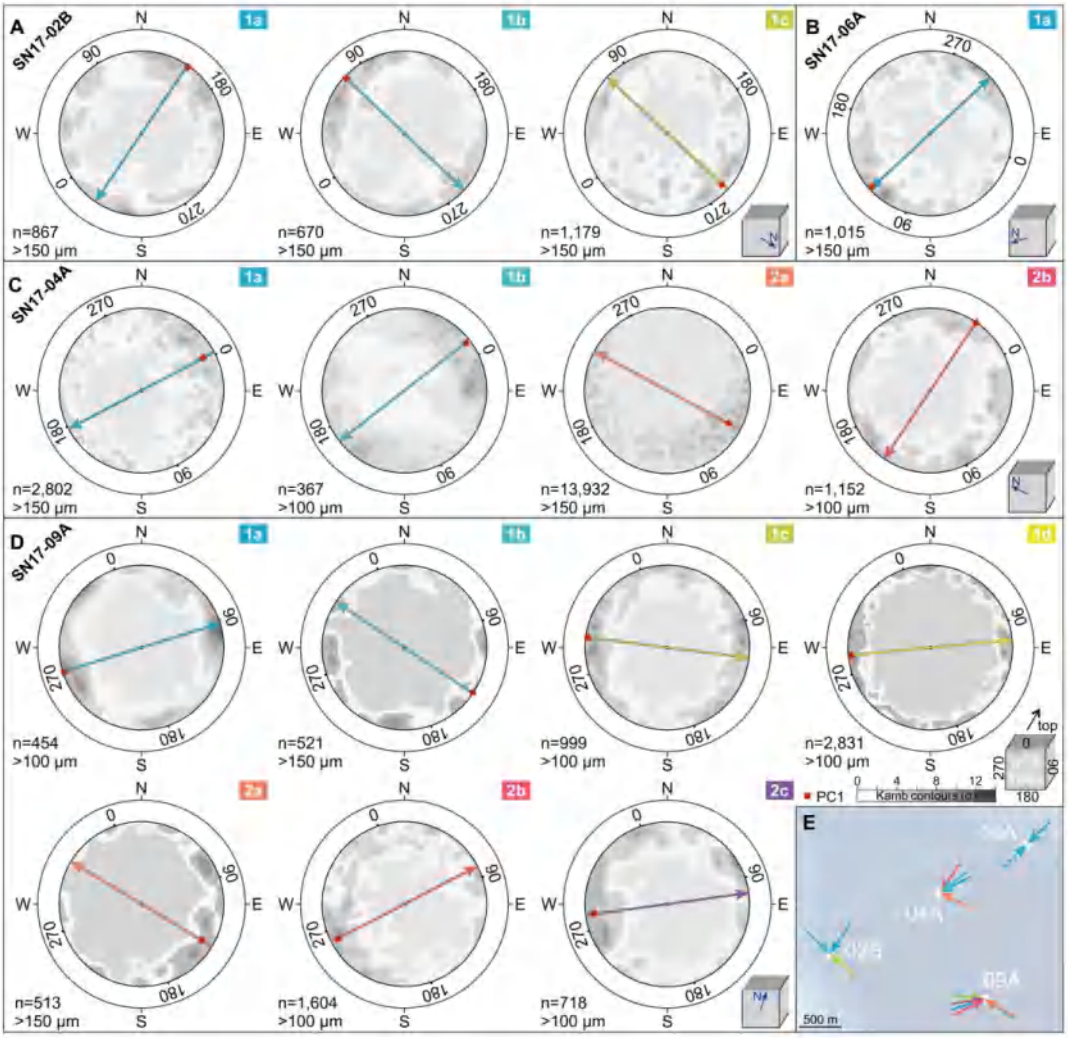

Figure 3. (A–D) Lower-hemisphere stereoplots showing plunge and trend of strongly elongated grains derived from high-resolution X-ray computed tomography (µCT) data analysis and measured with respect to the basal plane for each pulse in the 2007 CE seismo-turbidite from four cores in Lake Singkarak (West Sumatra; see Fig. 3). Each stereoplot, in µCT reference frame of the U-channel, is rotated so that geographic north is oriented to the figure top (see U-channel bottom view insets and compare to Figure 2). Considered grain sizes and total number of grains (n) are indicated at the bottom-left of each plot. Contour lines (Kamb, 1959) and Bingham axial distribution analysis

(Fisher et al., 1987) show main orientation in each data set (principal component, PC1, red square) and indicate flow direction (colored arrows). Flow sense was derived by considering dominant imbrication as up-current dipping. (E) Geographical context of resulting flow directions at each core site (see Fig. 1B). Dashed arrow for core SN17–06A indicates unlikely flow direction that cannot be ruled out with available data.

2. 海平面上升和下降控制了 Santorini 火山喷发活动

翻译人：冯婉仪 fengwy@sustech.edu.cn

Satow C, Gudmundsson A, Gertisser R, et al. ***Eruptive activity of the Santorini Volcano controlled by sea-level rise and fall****[J]. Nature Geoscience, 2021, 14: 586-592.*

https://doi.org/10.1038/s41561-021-00783-4

摘要：海平面的变化被认为是影响冰期到间冰期时间尺度上火山爆发的频率。然而，潜在的物理过程及其相对于其它影响（如：岩浆补给速率）的重要性仍然知之甚少。在这里，我们将位于希腊 Santorini 地区被淹没的破火山口的长达~ 360 kyr 的溢流式和爆发式喷发的记录与跨越最后四个冰期—间冰期旋回的高分辨率海平面记录进行比较。数值模拟表明，当海平面比现在的海平面下降 40 m 时，Santorini 岩浆房顶部由此产生的张应力会导致岩脉注入。随着海平面继续下降到−70 m 或−80 m，诱发的张应力扩散到整个岩浆房顶部，使得一些岩脉到达地面，为火山喷发提供动力。同样，当海平面上升到−40 m 以上时，火山活动逐渐消失。利用海洋沉积物岩心中的火山熔岩层，将 Santorini 地层与海平面记录同步，结果显示，211 次喷发（包括溢流式和爆发式）中有 208 次发生在海平面下降（低于−40 m）和随后上升的时期，这表明海平面对 Santorini 火山喷发的时间有很强的绝对控制作用—这个结果可能适用于世界上许多其它火山岛。

ABSTRACT: Sea-level change is thought to influence the frequencies of volcanic eruptions on glacial to interglacial timescales. However, the underlying physical processes and their importance relative to other influences (for example, magma recharge rates) remain poorly understood. Here we compare an approximately 360-kyr-long record of effusive and explosive eruptions from the flooded caldera volcano at Santorini (Greece) with a high-resolution sea-level record spanning the last four glacial–interglacial cycles. Numerical modelling shows that when the sea level falls by 40 m below the present-day level, the induced tensile stresses in the roof of the magma chamber of Santorini trigger dyke injections. As the sea level continues to fall to −70

or −80 m, the induced tensile stress spreads throughout the roof so that some dykes reach the surface to feed eruptions. Similarly, the volcanic activity gradually disappears after the sea level rises above −40 m. Synchronizing Santorini's stratigraphy with the sea-level record using tephra layers in marine sediment cores shows that 208 out of 211 eruptions (both effusive and explosive) occurred during periods constrained by sea-level falls (below −40 m) and subsequent rises, suggesting a strong absolute sea-level control on the timing of eruptions on Santorini—a result that probably applies to many other volcanic islands around the world.

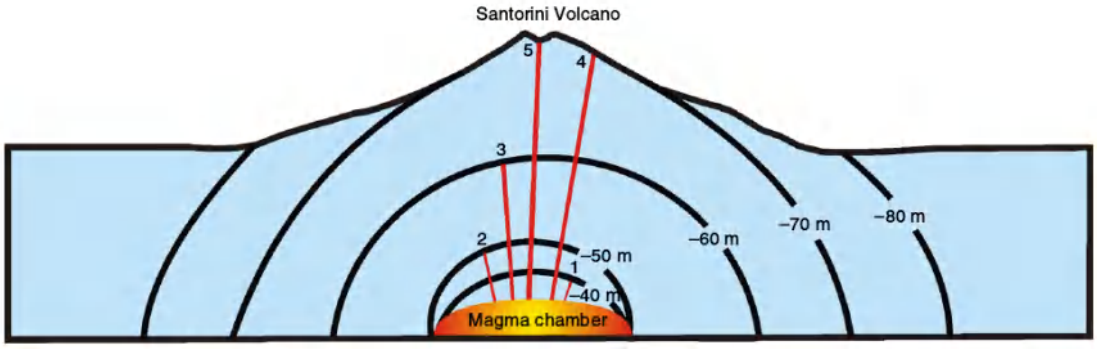

Figure 1. Schematic representation of the effect of sea-level-induced tensile stress spreading on the propagation of dykes at Santorini Volcano. The limits of the zones (marked by black semicircular/semi-elliptical curves) within which induced tensile stresses favour dyke propagation for a given sea level are indicated. The propagation paths of five dykes (red straight lines), numbered 1 to 5, are shown. When the sea level has fallen to −40 m, the induced tensile stress is limited to a semi-elliptical zone close to the chamber (the outer boundary of the zone is the −40 m curve) and all injected dykes (represented by dyke 1) are arrested. When the sea level falls further, tensile stress spreads through the roof of the chamber, but at −50 m and −60 m the outer boundaries of the high-tensile stress zones are still well below the surface, so the injected dykes (represented by dykes 2 and 3) are arrested. However, when the sea level falls to −70 m and, particularly, −80 m, the induced tensile stresses reach the surface of the volcano, and dyke-fed eruptions (represented by dykes 4 and 5) begin.

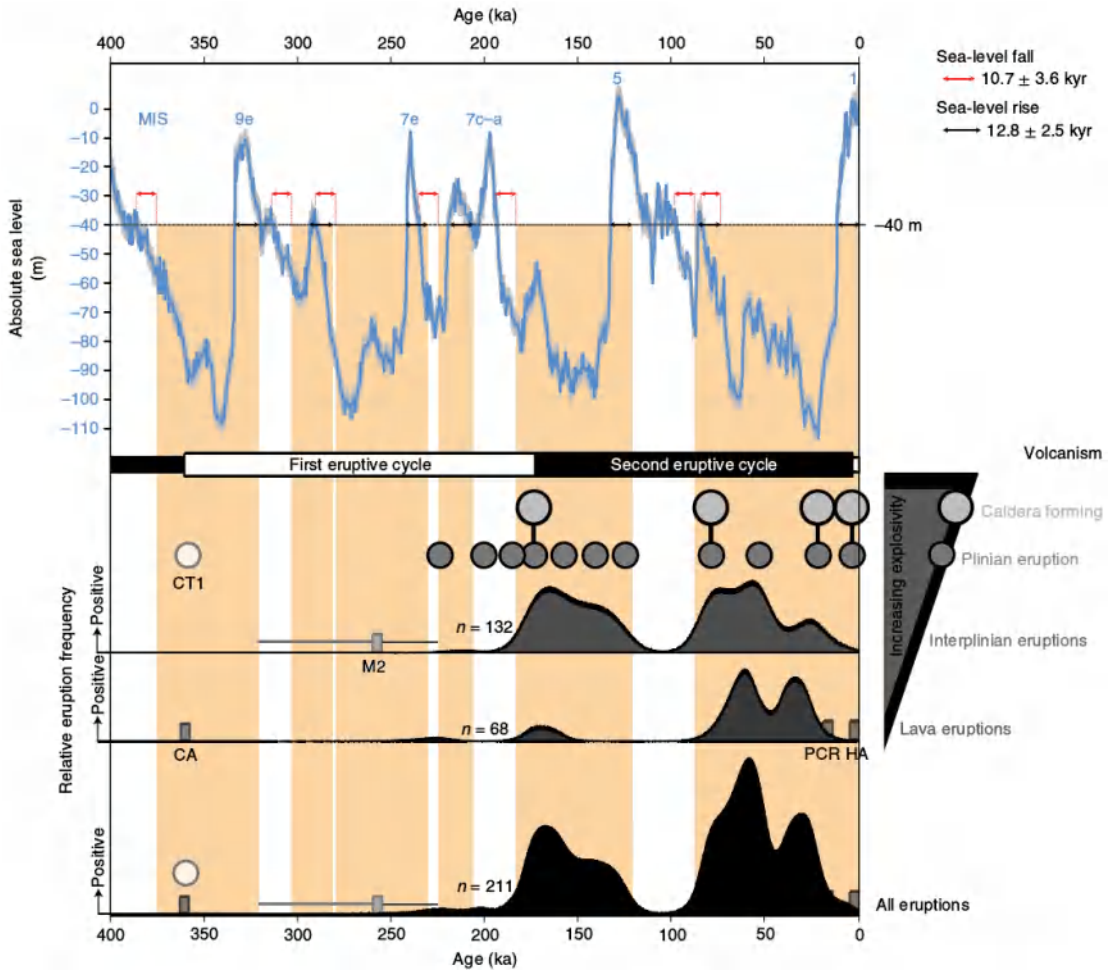

Figure 2. Santorini's eruptive stratigraphy aligned with absolute sea level. Top: absolute sea level (blue line) and 95% confidence interval (grey envelope)[23,24]. MIS is Marine Isotope Stage. Time lags between the sea level falling or rising through −40 m and the start or end of eruptive activity are denoted by red and black arrows, respectively. Vertical orange shading indicates time periods where our model implies that eruptions may be attributed to changes in tensile stress caused by sea-level changes. MIS, marine isotope stage. Bottom: Eruptive time series for Plinian, interplinian and lava eruptions as indicated in order of explosivity by the labels on the triangle on the right, with all eruptions combined on the lowermost panel. Caldera forming events associated with Plinian eruptions are indicated by light grey circles. Where both the chronology and the number of eruptions are well constrained, the eruption time series are represented by kernel density estimates (KDEs) (grey/back) with the number of events of each type shown (total n= 211). Where the number of events is either difficult to determine or the dating is very imprecise, eruptive events have been represented by grey boxes or white circles (most likely date) with whiskers for the error (if known). The height of the boxes does not imply the number of events. These events are labelled to allow

simple reference to the existing literature. CT1, Cape Therma 1; CA, Cape Alai lavas; M2, interplinian deposits[45,46]; PCR, post Cape Riva lavas; HA, historical activity. The time periods of the eruptive cycles that are traditionally used to describe the cycles in composition and style of Santorini's eruptions are also shown.

3. 一种基于火山灰的方法将地球磁场相对强度叠加结果校准为绝对值

翻译人:李园洁 liyj3@sustech.edu.cn

Mochizuki N, Fujii S, Hasegawa T, et al. ***A tephra-based approach to calibrating relative geomagnetic paleointensity stacks to absolute values****[J]. Earth and Planetary Science Letters, 2021, 572: 117119.*

https://doi.org/10.1016/j.epsl.2021.117119

摘要：相对古强度（RPI）叠加结果可提供能反映地心轴向磁偶极矩变化的相对的全球地磁场古强度的变化。过去对 RPI 叠加结果的校准是将平均 RPI 调整到从绝对强度数据库获得的虚轴向偶极矩（VADM）的平均值。为获得更定量化的将 RPI 叠加结果到绝对值的校准，本文我们提出一种新的方法：在氧同位素地层中，比较火山灰得到的绝对强度和相同火山灰层的相对强度（命名为“TA-TOR”方法）。对于该方法，APIs 是由 15 个日本火山碎屑流沉积物的凝灰岩确定。15 个新得到的 APIs 中的八个和两个之前报道的 APIs 在氧同位素地层有火山灰层。根据 TA-TOR 方法的 10 个数据并结合 4 个过渡场的数据，APIs 计算出的 VADMs 与同时期的 RPIs 叠加结果（PISO-1500 和 Sint-2000）进行比较。RPIs vs. VADMs 图中的 14 个数据表现为线性关系，相关系数为 0.83-0.89。利用观测到的线性关系，两个 RPIs 叠加曲线可靠地校准到过去 1.1 Ma 的 VADM 值。比较之前研究校准的 VADMs，现在校准值平均值低 12-13%，具有更大的分散度，两个 RPIs 叠加曲线的标准差高 15-53%。两个叠加曲线得到 $VADM_{API}$ 的累积分布与 API 数据库得到 VADMs 的相似，表明目前校准的可靠性。这些结果表明利用 TA-TOR 方法可以准确将 RPI 叠加结果转换为 $VADM_{API}$ 值，可为地心轴向偶极矩，沉积物 RPI 和宇宙放射性核素随时间变化的研究做出贡献。通过目前的校准，从 PISO-1500 和 Sint-2000 得到的过去 1.1 Ma 的 $VADM_{API}$ 的变化可作为这期间地心轴向偶极子变化的标准。

ABSTRACT: Relative paleointensity (RPI) stacks provide a relative, global paleointensity variation, which reflects variations in the geocentric axial dipole moment.

Previous calibrations of an RPI stack rely on adjusting a mean RPI to a mean of virtual axial dipole moments (VADMs), which are selected from absolute paleointensity (API) databases. To achieve more quantitative calibration of an RPI stack into absolute values, we propose a novel approach that compares (1) tephra-derived APIs and (2) the same tephras' horizons, in the oxygen isotope stratigraphy, tied RPIs (hereafter termed the "TA-TOR" approach). For the TA-TOR approach, APIs were newly determined for welded tuffs of 15 pyroclastic flow deposits in Japan. Eight of the 15 new APIs and 2 previously reported APIs have tephra horizons in the oxygen isotope stratigraphy. Based on the 10 data of the TA-TOR approach, combined with 4 data of the transitional field, VADMs calculated from the APIs ($VADM_{API}$) were compared with isochronous RPIs from two RPI stacks, PISO-1500 and Sint-2000. The 14 data points in RPI vs. ($VADM_{API}$ diagrams show a linear relationship with correlation coefficients of 0.83–0.89. Using the observed linear relationships, the two RPI stacks were reliably calibrated to VADM values (($VADM_{API}$) for the period since 1.1 Ma. Compared with the VADMs calibrated by the previous studies, the present calibration provides a 12–13% smaller median/mean and a larger dispersion as represented by a 15–53% larger standard deviation for the two RPI stacks. The similarities between the cumulative distributions of $VADM_{RPI}$ from the two stacks and those of VADMs selected from the API database indicate the reliability of the present calibration. These results show that the present calibration, which relies on the TA-TOR approach, accurately converts a RPI stack into $VADM_{RPI}$ values and will contribute to studies on time variations in the geocentric axial dipole moment, sedimentary RPI, and cosmogenic radionuclides. Variations in $VADM_{RPI}$ for the past 1.1 Myr, obtained from PISO-1500 and Sint-2000 via the present calibration, can be used as standard geocentric axial dipole variations for this period.

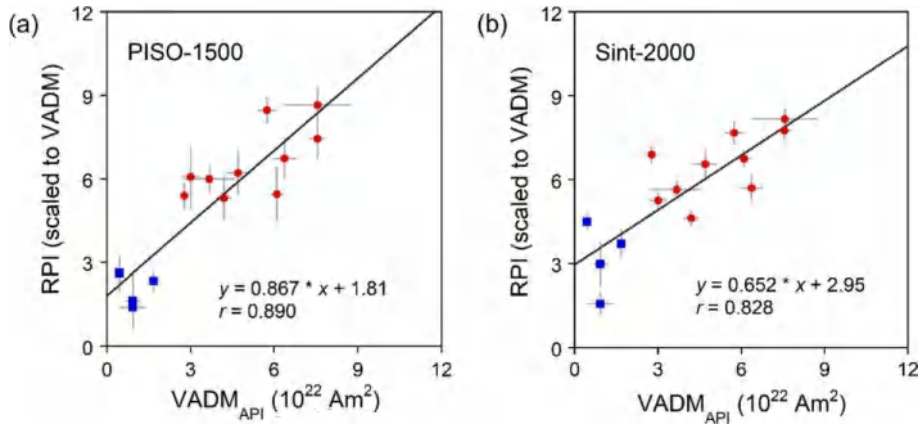

Figure 1. Comparison between absolute paleointensities (APIs) and relative paleointensities (RPIs) at well-constrained stratigraphic levels for (a) the PISO-1500 stack and (b) Sint-2000 stack. Comparison between $VADM_{API}$ and RPI was made at 14 stratigraphic levels which are indicated in Fig. 5: 10 tephrostratigraphic correlations (red circles) and 4 paleointensity lows in the transitional geomagnetic field (blue squares). Error bars for $VADM_{API}$ denote one standard deviation and those for RPI indicate one standard error, respectively. The solid line denotes the linear regression line for the data points.

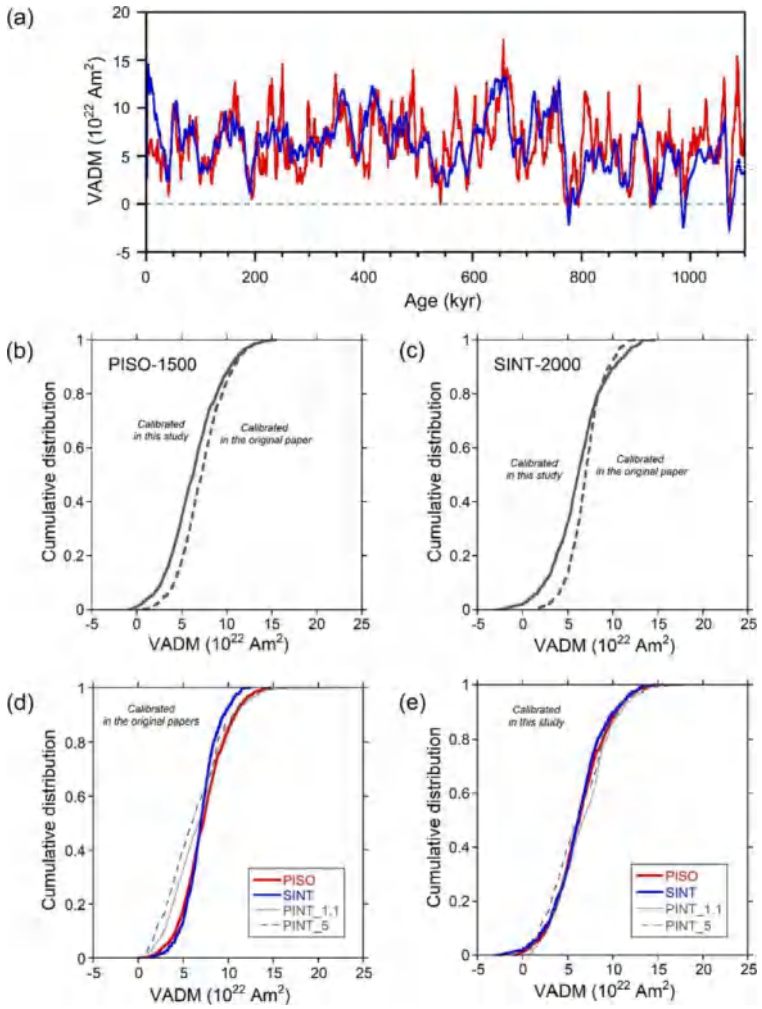

Figure 2. Variations in VADMs and cumulative distributions of the VADMs. (a) Variations in VADM (calibrated in the present study) derived from the RPI stacks for the past 1.1 Myr. The red line denotes the variation in VADM calibrated from the PISO-1500 stack, referred to as "VADM-1100-PISO." The blue line indicates the variation in VADM calibrated from the Sint-2000 stack, referred to as "VADM-1100-Sint." (b) Cumulative distribution of VADMs for the past 1.1 Myr derived from the PISO-1500 stack, which were calibrated in Channell et al. (2009) (dashed line), and that of VADMs calibrated in the present study (solid line). (c) The same figure as (b) derived from the Sint-2000 stack, which were calibrated in Valet et al. (2005) (dashed line), and that of VADMs calibrated in the present study (solid line). (d) Cumulative distributions of VADMs for the past 1.1 Myr, which were calibrated in the previous studies (red line: PISO-1500; blue line: Sint-2000). (e) Cumulative distributions of VADMs calibrated in the present study. Cumulative distributions of VADMs for the past 1.1 and 5 Myr calculated using the selected API data from the PINT database are also shown in Fig. 7d and e (thin, solid and dashed lines).

4. 月球没有长期古磁层

翻译人：柳加波 liujb@sustech.edu.cn

Tarduno J A, Cottrell R D, Lawrence K, et al. ***Absence of a long-lived lunar paleomagnetosphere****[J]. Science Advances, 2021, 7(32): eabi7647.*

https://doi.org/10.1126/sciadv.abi7647

摘要：月球古磁场是否长期存在对了解月球深部和月表演化至关重要。本文研究了两百万年前陨石撞击坑的阿波罗玻璃质样品，该样品记录了类似地球的高磁化强度。但是两百万年前月球不存在核心磁场，这表明撞击会导致来自月球和其他星体的样品携带很强的剩磁。此外，我们发现那些大约 39、36、33 和 32 亿年前形成的阿波罗样品中含有磁性包裹体的硅酸盐晶体能够，但是没有记录类似地核发电机的磁场。综上，这表明月球不存在一个持续的古磁层保护，月球表土应该埋藏着 ^{3}He、水和其他在约 40 亿年间从太阳风和地球磁层中获得的挥发性资源。

ABSTRACT: Determining the presence or absence of a past long-lived lunar magnetic field is crucial for understanding how the Moon's interior and surface evolved. Here, we show that Apollo impact glass associated with a young 2 million–year–old crater records a strong Earth-like magnetization, providing evidence that impacts can impart intense signals to samples recovered from the Moon and other planetary bodies. Moreover, we show that silicate crystals bearing magnetic inclusions from Apollo samples formed at ~3.9, 3.6, 3.3, and 3.2 billion years ago are capable of recording strong core dynamo–like fields but do not. Together, these data indicate that the Moon did not have a long-lived core dynamo. As a result, the Moon was not sheltered by a sustained paleomagnetosphere, and the lunar regolith should hold buried 3He, water, and other volatile resources acquired from solar winds and Earth's magnetosphere over some 4 billion years.

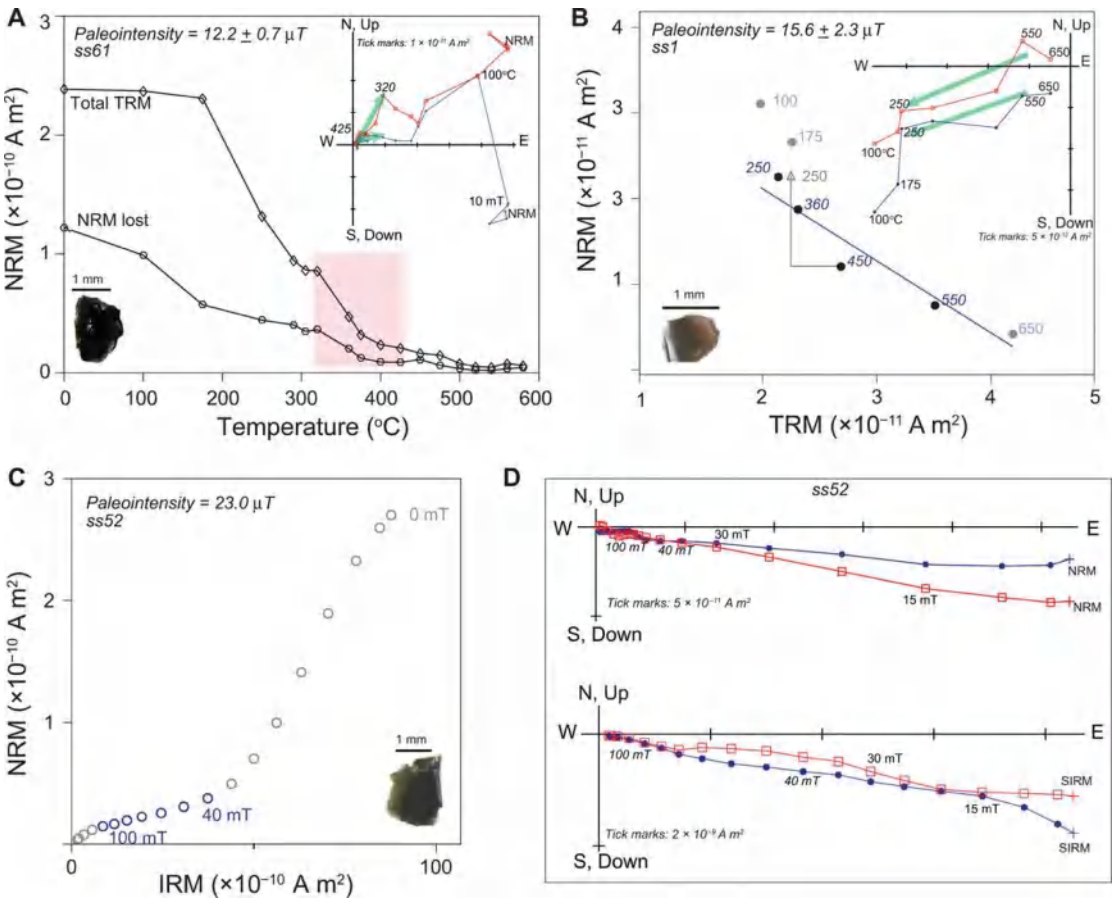

Figure 1. Paleointensity analyses on Apollo 64455 glass. Subsamples measured are shown as inset in (A to C). (A) TTRM experiment. Plot of the decay of NRM and laboratory-induced TTRM with temperature. The pink shaded region represents steps used to determine the paleointensity value. The inset shows the orthogonal vector plot of NRM demagnetization. A three-point sliding window average was used to reduce noise in the remanence signal and determine the characteristic remanent magnetization (ChRM) using principal components analysis (green arrows). Red, inclination (vertical) component; blue, declination (horizontal) component. (B) Thellier-Coe paleointensity experiment. The loss of NRM is plotted against the acquisition of a laboratory-induced TRM (circles) and (pTRM) check (triangle). Black circles/blue labels identify data used to fit paleointensity. The inset shows orthogonal vector plot of field-off steps. Conventions as in (A). Labels in italics identify temperature range used in paleointensity fit. (C and D) REM' paleointensity determination. (C) The loss of NRM plotted against loss of IRM. (D) Orthogonal vector plot of AF demagnetization of NRM (top) and 3-T saturating IRM (bottom); conventions as in (A). The slope of the line in (C) that matches the AF range, where the ChRM is defined in the NRM orthogonal vector plot [40 to 100 mT in (D)], is related to the paleofield strength by a calibration factor (see Materials and Methods).

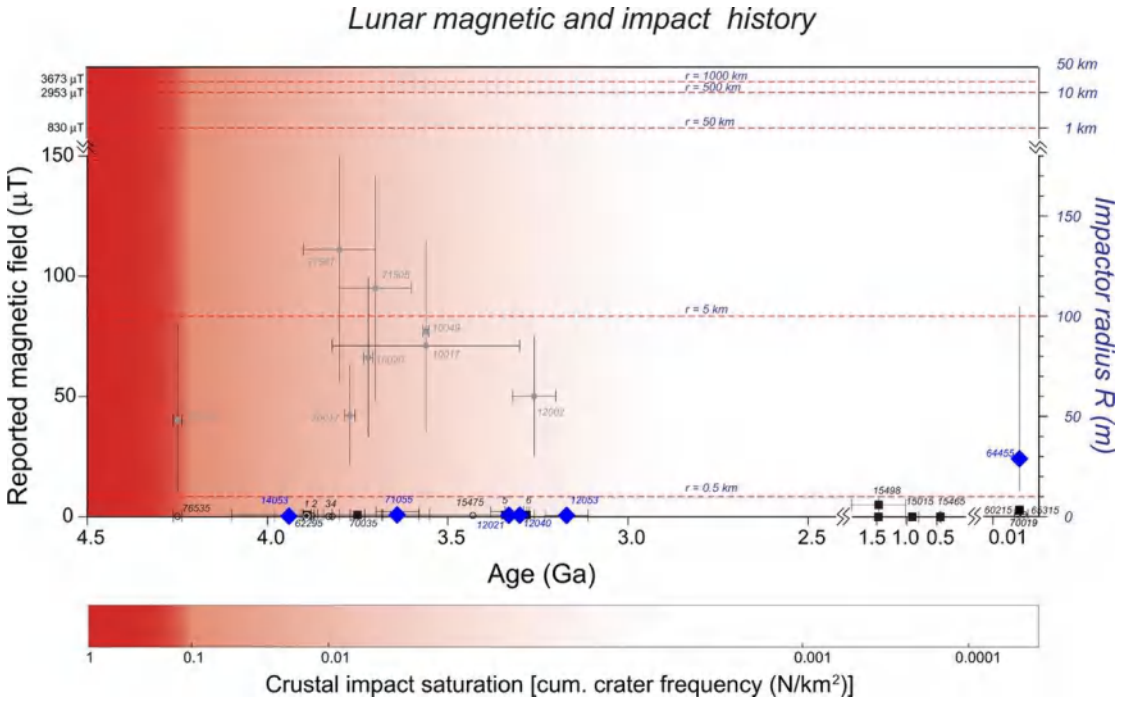

Figure 2. Lunar magnetic and impact history. Reported field strength measurements from select Apollo samples (table S5) shown as follows: gray filled circles, nonthermal methods; open circles, no evidence for primary remanence, interpreted as magnetic contamination or results of magnetic interactions/phase changes during analysis; black squares, data based on thermal analyses. All sample numbers are listed except the following: 1, 68815 (open circle); 2, 62235; 3, 72215; 4, 75055; 5, 60015 (black square); and 6, 15016. Blue diamonds, thermal analysis values (this work). The right axis shows field impactor radius (R) capable of generating the field intensities by magnetizations induced by charge separation. Radius (r) values shown by dashed lines are field values at $r = 50R$. The shaded region reflects the degree of crustal impact saturation (see Materials and Methods).

5. 阿曼成冰纪 Fiq 组的旋回地层学及其对马里诺冰川化时间的约束

翻译人：盖聪聪 gaicc@sustech.edu.cn

Gong Z. ***Cyclostratigraphy of the Cryogenian Fiq Formation, Oman and its implications for the age of the Marinoan glaciation****[J]. Global and Planetary Change, 2021(204).*

https://doi.org/10.1016/j.gloplacha.2021.103584

摘要：旋回地层学常用于年代学研究，在前寒武纪的研究中很有潜力。成冰纪是地球历史上最具活力且有趣的时期之一，两次雪球地球事件（最极端的气候变化）就发生在这时候。然而，我们对时间更近的雪球地球事件（马里诺雪球事件）的研究仍缺乏可靠的年龄框架，这阻碍了不同区域间的地层对比，也影响了我们对这个全球尺度冰川化事件起止的认识。阿曼地区成冰纪 Fiq 组的地层和马里诺地层时间一致，Fiq 组非成冰单元的持续时间可以用来保守估计马里诺冰川化开始的时间。在这项工作中，作者对 Fiq 组三个钻孔开展了旋回地层学研究，对高分辨率伽马数据进行了多窗谱分析法、相关系数和演化谱相关系数分析。作者在数据中识别出米兰科维奇周期（偏心率、斜率、岁差），这些周期被用于估算各钻孔的最优沉积速率和 Fiq 组的持续时间。分析结果显示，Fiq 组至少沉积了 6 百万年。结合放射性测年和其它区域的旋回地层数据，马里诺冰川化的起始时间应该在 650-641 百万年这一范围内。作者的这项研究改进了成冰纪的年代框架，为探索雪球地球事件可能机制的地质和数值方法提供了关键的时间约束。

ABSTRACT: Cyclostratigraphy is a powerful tool in chronostratigraphic studies, and has shown its potential in Precambrian time. The Cryogenian Period is one of the most dynamic and intriguing intervals in Earth history and it is a witness to the most extreme climate changes on the planet, known as two Snowball Earth events. However, a robust chronostratigraphic framework is still lacking especially for the younger Marinoan Snowball Earth event, hampering the stratigraphic correlation and comparison among geographically separated records, as well as the understanding of the initiation and termination of this global-scale glaciation. The Cryogenian Fiq Formation in Oman is

thought to be Marinoan-equivalent. The duration of the nonglacial units in the Fiq Formation could provide a conservative age constraint on the previously not well-determined onset age of the Marinoan glacia- tion. In this work, a cyclostratigraphic study has been conducted on three drill cores of the Fiq Formation. The multi-taper method (MTM) spectral analysis, the correlation coefficient (COCO), and the evolutionary correlation coefficient (eCOCO) analyses were performed on the high-resolution gamma-ray (GR) data from the three cores. A hierarchy of Milankovitch cycles (eccentricities, obliquities, and precessions) has been identified, which was used to estimate the optimal sedimentary accumulate rates and the duration of the Fiq Formation in each core. Based on the cyclostratigraphic results, the time scale of the Fiq Formation is at least ~6 Myr. Integrating the radiometric ages and the cyclostratigraphic data from other continents, the onset age of the Marinoan glaciation is suggested to be 650–641 Ma. This new result helps improve the chronostratigraphic framework for the Cryogenian Period and also provides critical temporal constraints for the geological and numerical models that explore the possible mechanisms for the Snowball Earth events.

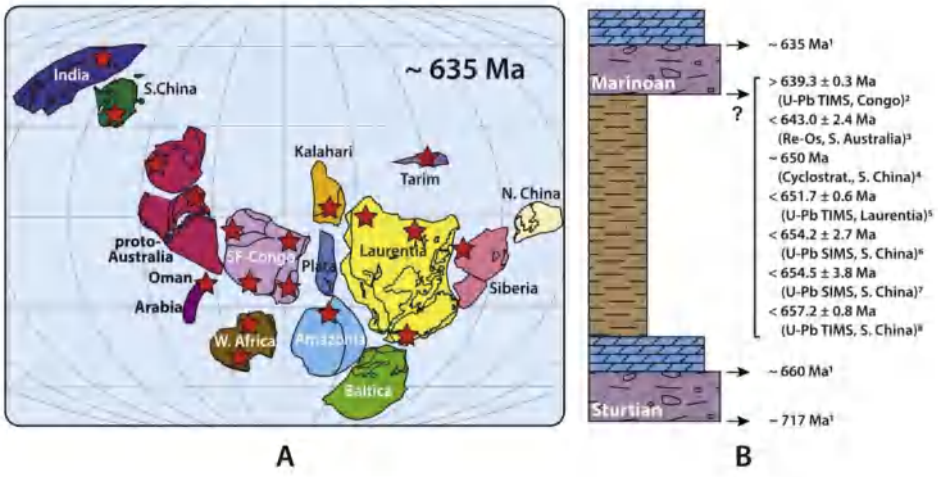

Figure 1. Paleogeographic reconstruction model is from Zhang et al. (2013) and Bao et al. (2018). The red stars represent the records of Marinoan glaciation compiled by Hoffman et al. (2017). (B) Available age constraints on the Cryogenian Snowball Earth events. Geochronological references: 1. Hoffman et al. (2017); 2. Prave et al. (2016); 3. Kendall et al. (2006); 4. Bao et al. (2018); 5. Nelson et al. (2020); 6. Lan et al. (2015); 7. Zhang et al. (2008); 8. Rooney et al. (2020).

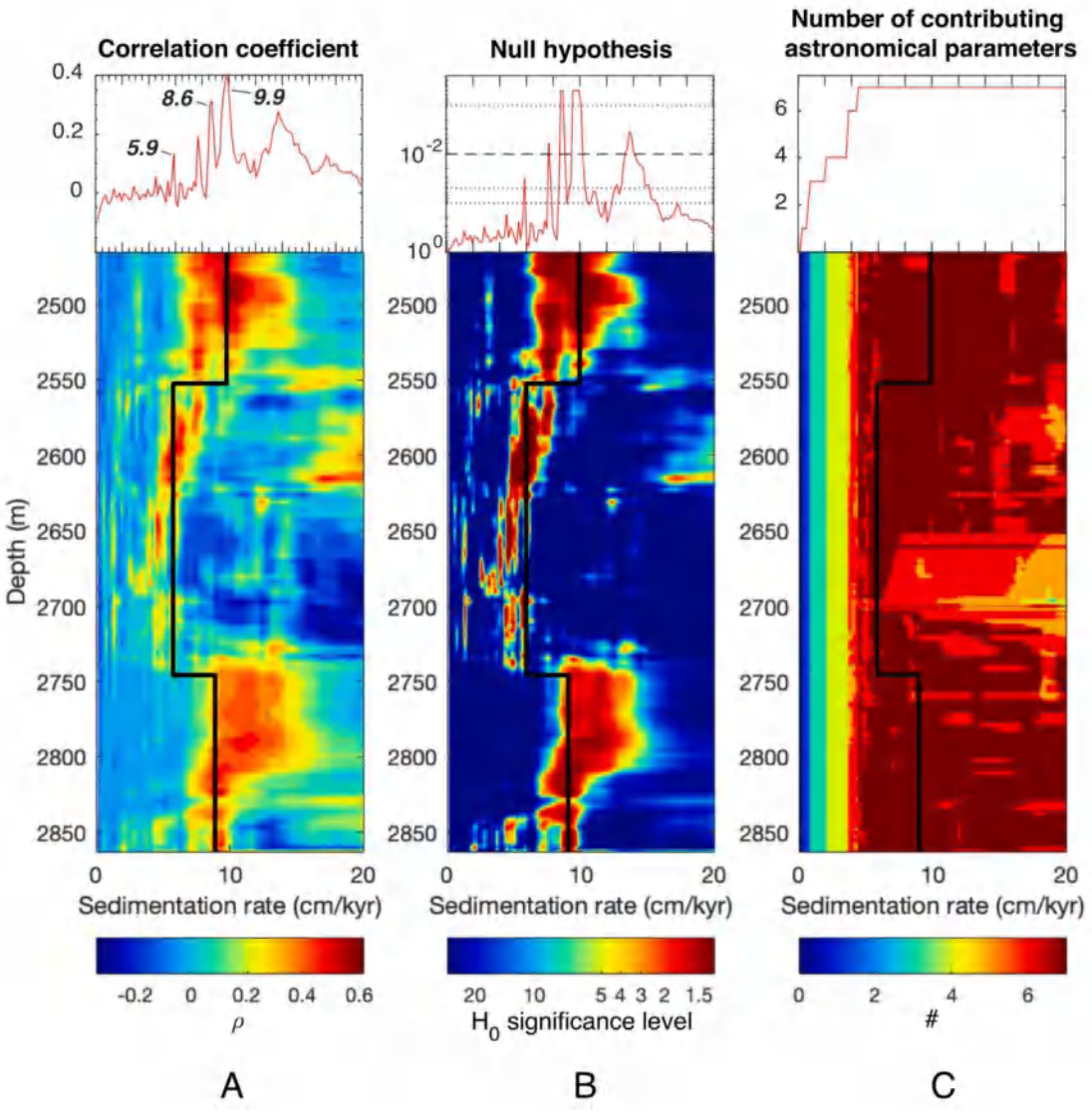

Figure 2. The COCO and eCOCO results of the Hathnar-1 core. (A) Correlation coefficient (top) and evolutionary correlation coefficient (bottom). (B) Null hypothesis (H_0, no astronomical forcing; top) and evolutionary H_0 significance level (bottom). (C) The number of contributing astronomical parameters (top) and evolutionary number of contributing astronomical parameters (bottom). The optimal SARs are indicated with numbers. The unit of SAR is cm/kyr. The black lines delineate the changes in SAR through the stratigraphy.

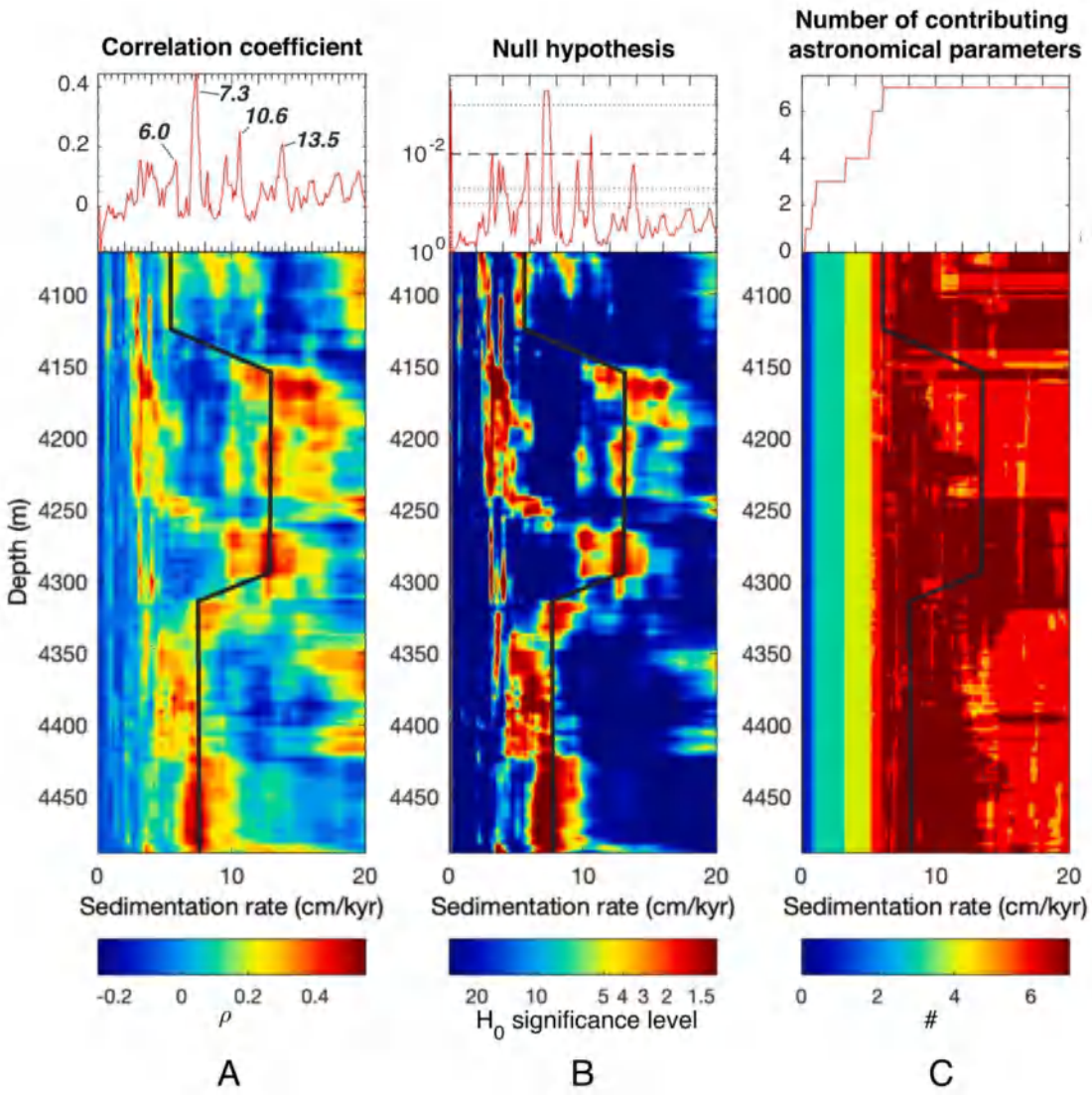

Figure 3. The COCO and eCOCO results of the Suwaihat-5H2 core. (A) Correlation coefficient (top) and evolutionary correlation coefficient (bottom). (B) Null hypothesis (H_0, no astronomical forcing; top) and evolutionary H_0 significance level (bottom). (C) The number of contributing astronomical parameters (top) and evolutionary number of contributing astronomical parameters (bottom). The optimal SARs are indicated with numbers. The unit of SAR is cm/kyr. The black lines follow the changes in SAR through the stratigraphy.

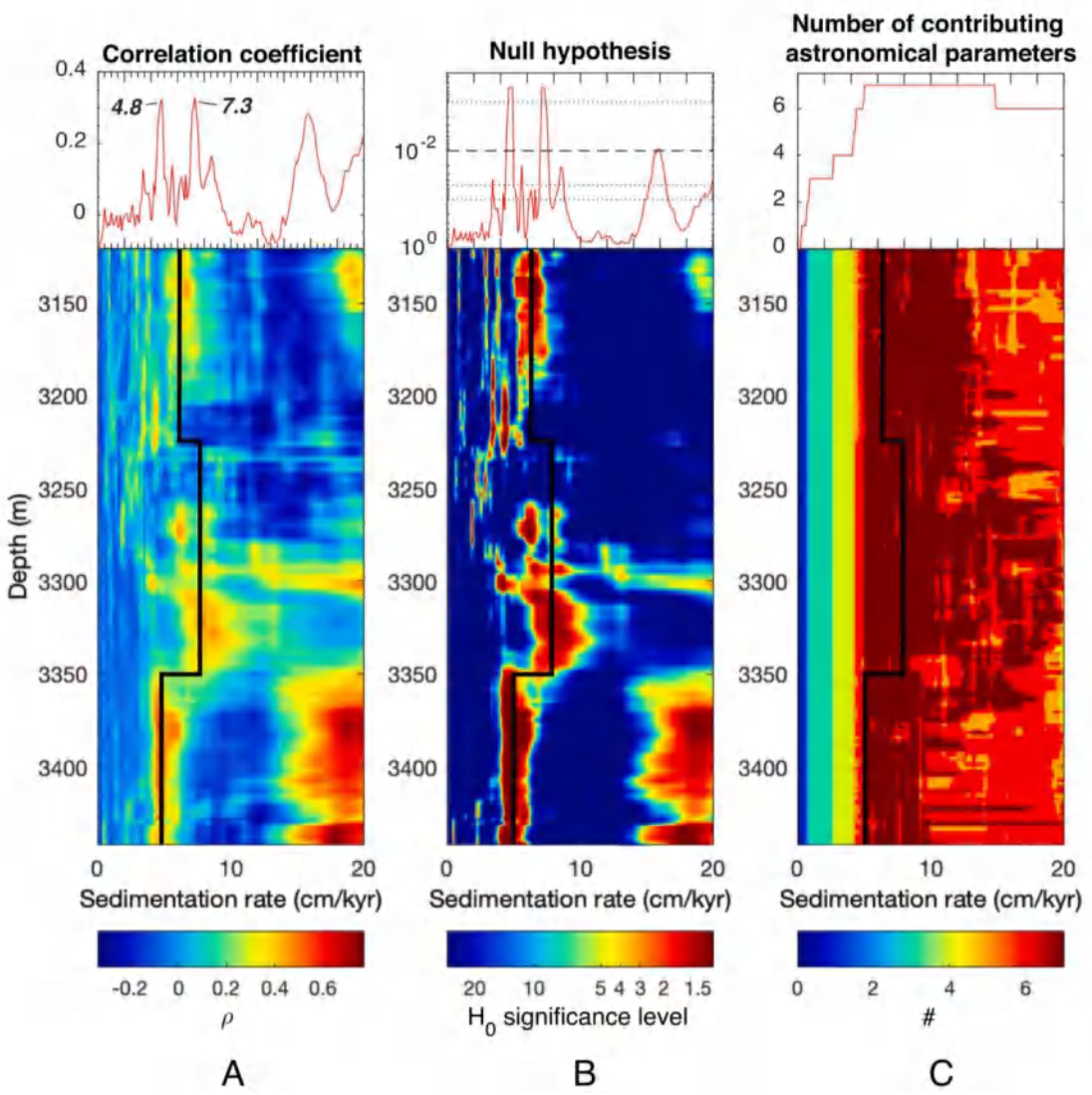

Figure 4. The COCO and eCOCO results of the Farha-1 core. (A) Correlation coefficient (top) and evolutionary correlation coefficient (bottom). (B) Null hypothesis (H_0, no astronomical forcing; top) and evolutionary H_0, significance level (bottom). (C) The number of contributing astronomical parameters (top) and evolutionary number of contributing astronomical parameters (bottom). The optimal SARs are indicated with numbers. The unit of SAR is cm/kyr. The black lines show the changes in SAR through the stratigraphy.

6. 始新世-渐新世转换时南半球陆地变冷由 pCO_2 降低引起

翻译人：蒋晓东jiangxd@sustech.edu.cn

Lauretano V, Kennedy-Asser A T, Korasidis V A, et al. ***Eocene to Oligocene terrestrial Southern Hemisphere cooling caused by declining pCO_2[J]****. Nature Geoscience, 2021.*

https://doi.org/10.1038/s41561-021-00788-z

摘要：西南太平洋和南极大陆边缘的海表温度变化很好的记录了始新世—渐新世（EO）期间从温室到冰室的气候转换，这一转换呈现出长时间尺度的持续变冷。然而对变冷事件是否出现在陆地的深入理解是鉴别该事件驱动机制的基础。本文中我们利用保存在澳大利亚东南部褐煤中的细菌分子化石，得到了从中始新世到早渐新世（~41 - 33 Ma）半连续的陆地温度记录。我们的结果揭示澳大利亚东南部的年平均温度从中始新世的~27 °C（± 4.7 °C）逐渐降低到晚中新世的~22 - 24 °C（± 4.7 °C），且在 EO~转换边界约为 2.4 °C 的降温步长。这一温度变化与南半球的其他记录一致，表明他们具有共同的驱动机制，例如 pCO_2。之后我们通过一整套气候模型的模拟，校正了这些温度记录，结果表明仅有 pCO_2 降低能引起澳大利亚东南部变冷。在南极冰期起始时段海陆相互作用和气候驱动背景下，我们的数据对检验气候模型性能形成了一个重要的基准。

ABSTRACT: The greenhouse-to-icehouse climate transition from the Eocene into the Oligocene is well documented by sea surface temperature records from the southwest Pacific and Antarctic margin, which show evidence of pronounced long-term cooling. However, identification of a driving mechanism depends on a better understanding of whether this cooling was also present in terrestrial settings. Here, we present a semi-continuous terrestrial temperature record spanning from the middle Eocene to the early Oligocene (~41 - 33 million years ago), using bacterial molecular fossils (biomarkers) preserved in a sequence of southeast Australian lignites. Our results show that mean annual temperatures in southeast Australia gradually declined from ~27 °C (±4.7 °C) during the middle Eocene to ~22 - 24 °C (±4.7 °C) during the late Eocene, followed by

a ~2.4 °C-step cooling across the Eocene/Oligocene boundary. This trend is comparable to other temperature records in the Southern Hemisphere, suggesting a common driving mechanism, likely pCO_2. We corroborate these results with a suite of climate model simulations demonstrating that only simulations including a decline in pCO_2 lead to a cooling in southeast Australia consistent with our proxy record. Our data form an important benchmark for testing climate model performance, sea - land interaction and climatic forcings at the onset of a major Antarctic glaciation.

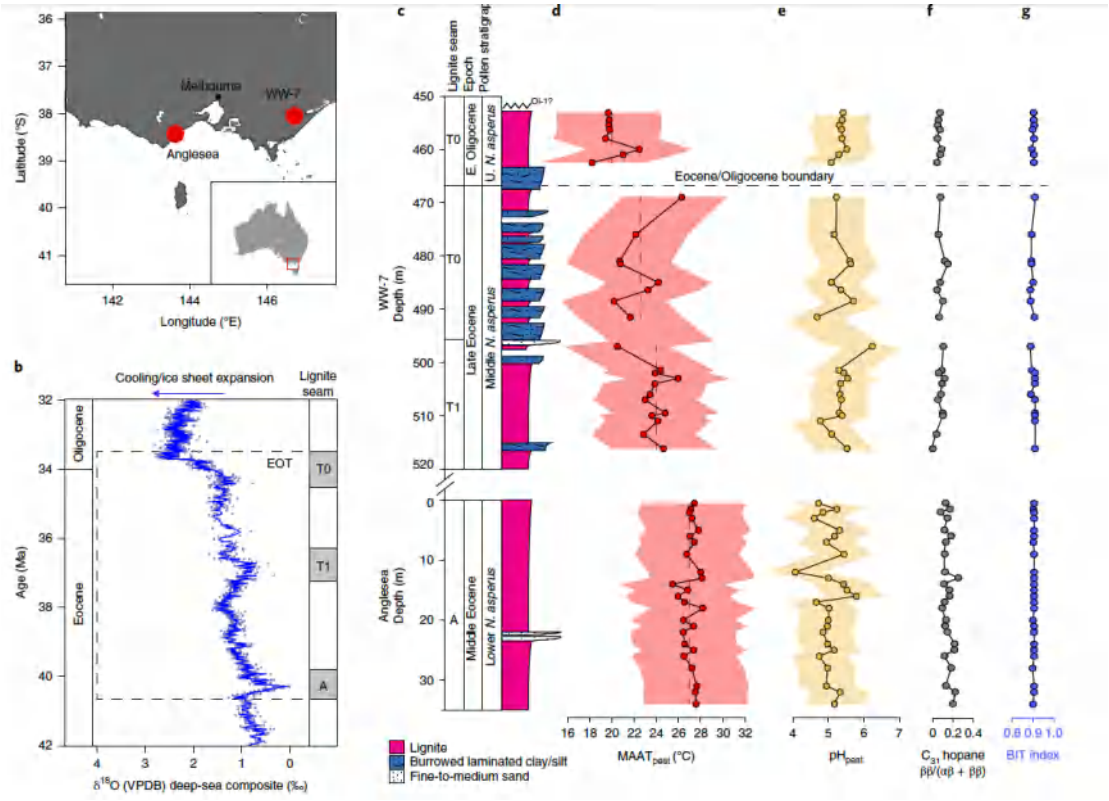

Figure 1. Middle Eocene to early Oligocene temperatures. a, Map of the locations of the Anglesea and WW-7 lignite seams in southeast Australia. b, Benthic foraminiferal $\delta^{18}O$ for ref. 1, expressed in VPDB (Vienna Pee Dee Belemnite), with the positions of the EOT and the relative ages of the Anglesea (A) and Traralgon (T1 and T0) seams indicated. c, Stratigraphic log of the Anglesea and Traralgon (WW-7 borehole) lignite seams, where pink indicates lignite. d, brGDGT-derived $MAAT_{peat}$ values. The dotted lines indicate average temperatures. e, brGDGT-derived pH_{peat} values. f, C_{31} hopane ββ/(αβ + ββ) ratio, with low values representative of an acidic peat depositional

environment. g, BIT index (measuring the relative abundance of archaeal isoprenoidal GDGTs over bacterial brGDGTs), with high values indicative of a terrestrial environment. The shading in d and e represents calibration errors. E, early; U, upper. Map in a: Ocean Data View (https://odv.awi.de/).

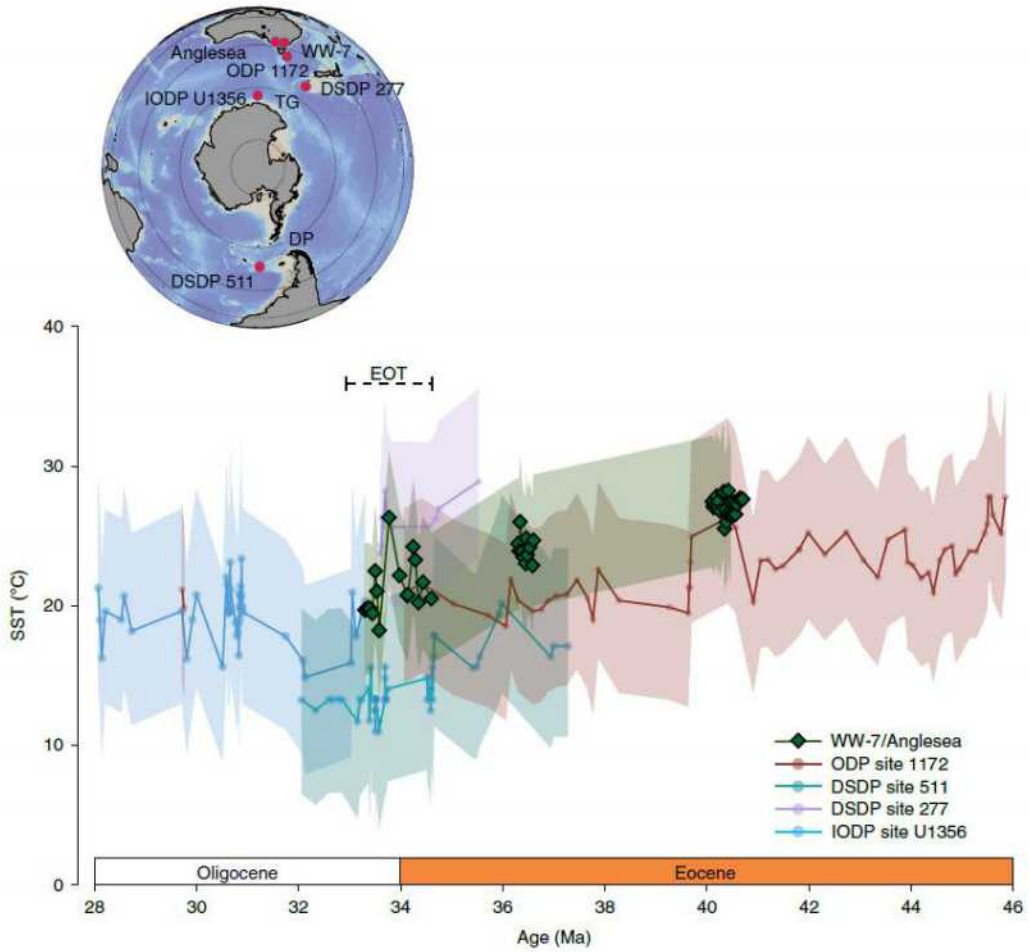

Figure 2. Terrestrial temperatures versus SSTs. Terrestrial MAATpeat values from the WW-7 borehole and Anglesea lignite seams from southeast Australia (this study) and published TEX86-based SSTs from the Southern Hemisphere (ODP Site 1172, DSDP Site 277, DSDP Site 511 and Integrated ODP (IODP) Site U1356) recalculated using BAYSPAR calibration. The error bars reflect calibration uncertainties. The position of the EOT is also indicated. Inset: locations of the SST and Australian sites, as well as the Tasman Gateway (TG) and Drake Passage (DP). Map: Ocean Data View (https://odv.awi.de/).

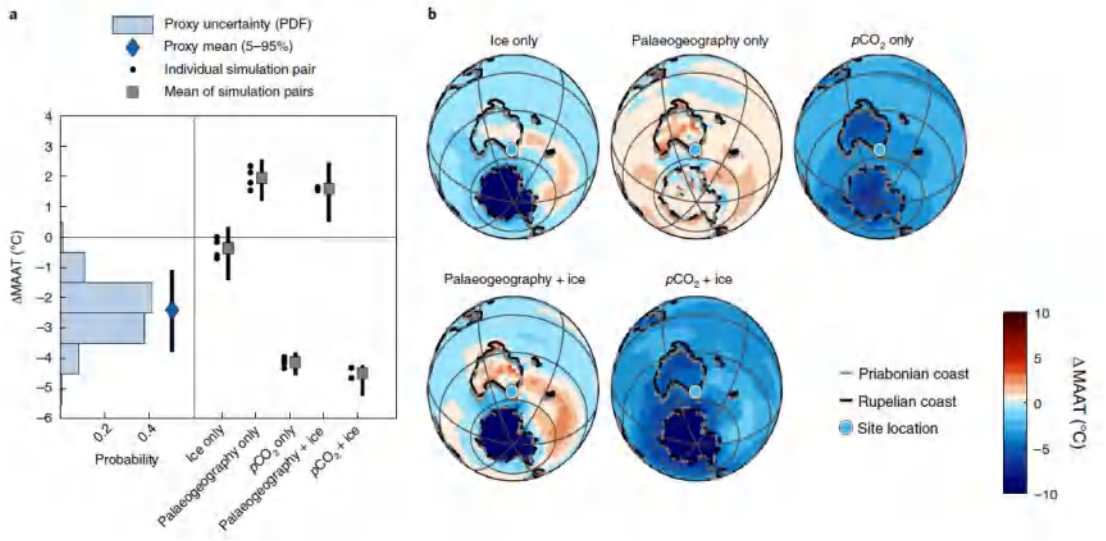

Figure 3. Comparison with climate model simulations. a, MAAT changes obtained from model simulations based on the different forcings (dots) against the temperature change observed in the $MAAT_{peat}$ record across the EOT. The blue diamond represents the mean change with ±90% uncertainty. The blue bars represent the spread-of-uncertainty distribution in calculating the temperature change in the proxy record. PDF is the probability density function. The squares represent the mean simulation response for each of the forcings, with error bars based on the spatial uncertainty. b, Multi-simulation mean responses to five EOT forcing scenarios. The lignite record presented here is shown by the blue dot.

7. 欧亚板块东北端 Izanagi -太平洋洋脊转换部位的俯冲

翻译人：周洋 zhouy3@sustech.edu.cn

Toru Y, Gen S, Kenichiro T, et al. ***Subduction of the Izanagi-Pacifc Ridge–transform intersection at the northeastern end of the Eurasian plate****[J]. Geology, 2021, 49, 952–957.*

https://doi.org/10.1130/G48611.1

摘要：最近对全球板块运动的重建表明，Izanagi-太平洋洋脊在大约 50 Ma 左右沿欧亚大陆东部边缘俯冲。在位于欧亚板块东北端的 Hidaka 岩浆带（HMZ）中，有三期岩浆活动（46-45 Ma、40-36 Ma 和 19-18 Ma）。我们报道了来自 HMZ 的 36 Ma 的高 Sr/Y（埃达克质）的岩石全岩地球化学和 Sr-Nd-Pb 同位素特征，表明这些岩石是由洋壳部分熔融形成的，并在洋脊俯冲过程中在近海沟的部位侵位。我们重新了解了 HMZ 中深成侵入体的性质，表明 46-45 Ma 和 40-36 Ma 的花岗岩具有相似的地球化学特征。45-40 Ma 之间的岩浆平静期可以很好地解释为洋脊转换部位的俯冲。始新世花岗岩之间的边界对应于古转换断层的位置，埃达克质岩浆是由扩张中心的板块撕裂引发的部分熔融形成的。古洋脊转换构造与后来的大断层和橄榄岩位置重合。

ABSTRACT: Recent reconstructions of global plate motions suggest that the Izanagi-Pacifc Ridge was subducted along the eastern margin of Eurasia at ca. 50 Ma. In the Hidaka magmatic zone (HMZ), which was located at the northeastern end of the Eurasian plate, three magmatic pulses occurred (46-45, 40-36, and 19-18 Ma). We report whole-rock geochemical and SrNd-Pb isotopic data for 36 Ma high-Sr/Y (adakitic) rocks from the HMZ and show that these rocks formed by partial melting of oceanic crust and were emplaced as near-trench intrusions during ridge subduction. We reevaluate the nature of plutonic rocks in the HMZ and show that both the 46-45 and 40-36 Ma granitoids have essentially identical geochemical features. The distribution of plutons and magmatic cessation between 45 and 40 Ma are best explained by subduction of a ridge-transform intersection with a large offset of the ridge axis. The

boundary between the Eocene granitoids corresponds to the position of a paleo–transform fault, and adakitic magmatism was caused by partial melting triggered by slab tearing at an overlapping spreading center. The paleoridge-transform confguration coincides with the locations of later large faults and a peridotite body.

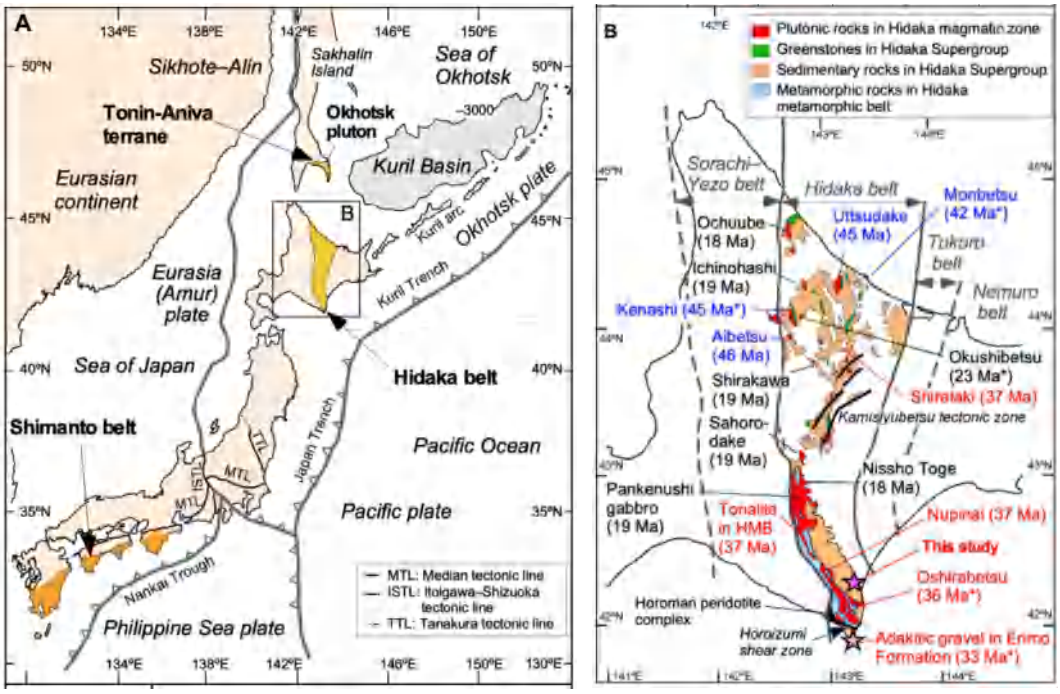

Figure 1. (A) Present day tectonic framework around Japan. (B) Tectonic and geological map with reported age data for plutonic rocks of central Hokkaido. The blue, red, and black characters with ages are products of 46-45 Ma, 37-36 Ma, and 19-18 Ma magmatism, respectively. Ages marked with asterisk are K-Ar biotite ages, and other ages are zircon U-Pb ages (data sources are given in the Supplemental Material [see footnote 1]). Hidaka, Shimanto, Sorachi-Yezo, Tokoro, and Nemuro belts denote names for geotectonic units in Japan. HMB—Hidaka metamorphic belt.

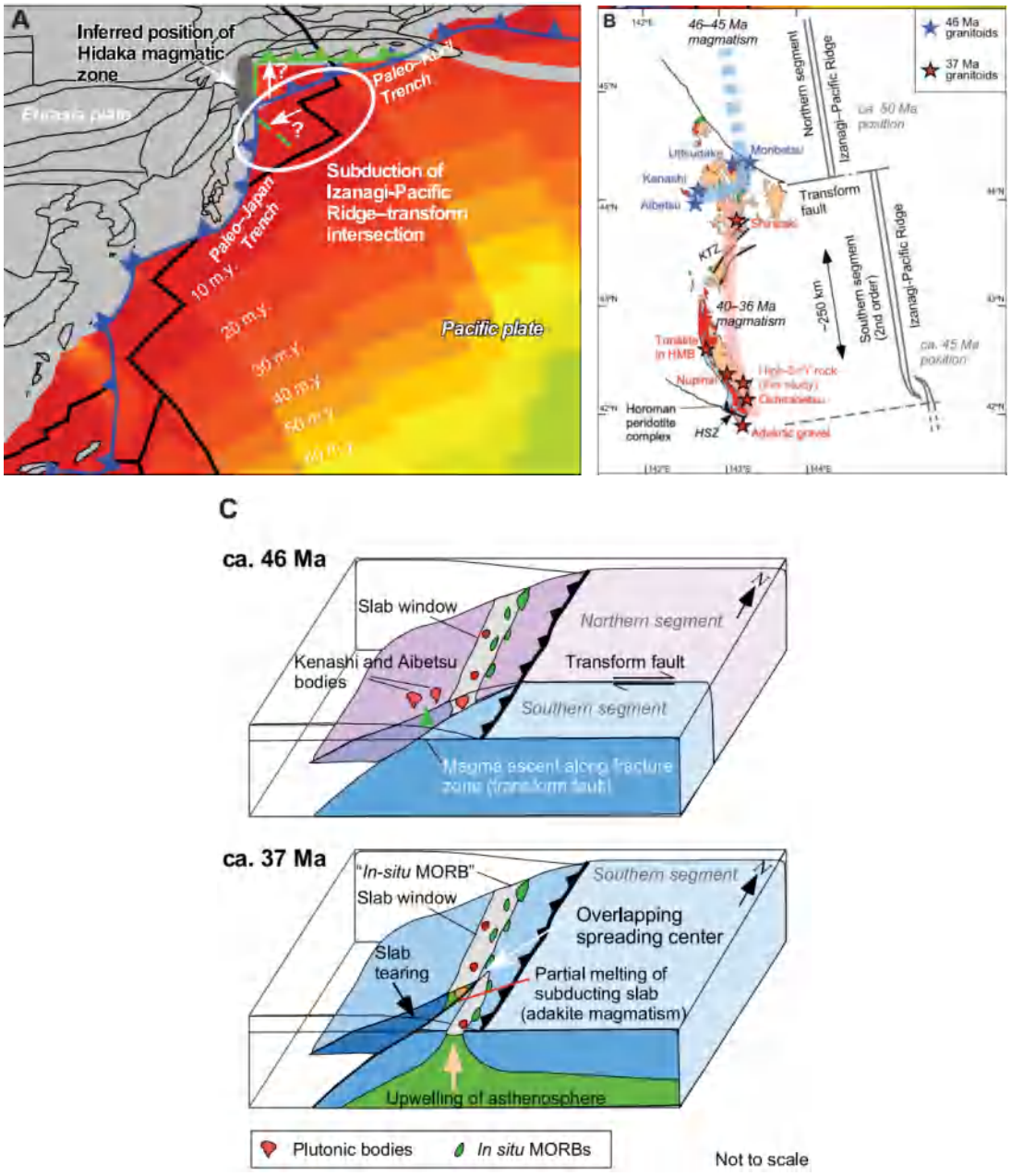

Figure 2. Schematic illustrations showing geodynamic setting of the subduction of the Izanagi-Pacific Ridge-transform intersection in the Eocene. (A) Reconstructed map of the subducting Izanagi-Pacifc Ridge at 57 Ma generated by GPlates software (Müller et al., 2016, 2018) and the inferred position of the Hidaka magmatic zone (dark gray). Blue line with triangles is trench. Light gray area denotes the Eurasia plate. Various colors in the oceanic plates represent age of oceanic plate at 10 m.y. interval. Compared with the synthetic global model of Müller et al. (2016), our geological model infers a somewhat western location for the large transform fault (dashed green line) or a northern location for the paleo-Kuril Trench (solid light green line with triangles). (B) Distribution of Eocene granitoids and inferred Izanagi-Pacifc Ridge segment at ca. 50 and 45 Ma.

HMB-Hidaka metamorphic belt; KTZ-Kamisiyubetsu tectonic zone; HSZ-Horoizumi shear zone. (C) Schematic tectonic model showing magmatism at ca. 46 and 37 Ma. MORB-midoceanic ridge basalt.

8. 台湾西部麓山带和雪山山脉沉积物的物源:基于 EMP 独居石与 LA-ICPMS 碎屑颗粒锆石年代学的新观点

翻译人：刘伟 inewway@163.com

Chen C H, Lee C Y, Lin J W, et al. ***Provenance of sediments in western Foothills and Hsuehshan Range (Taiwan): A new view based on the EMP monazite versus LA-ICPMS zircon geochronology of detrital grains****[J]. Earth-Science Reviews, 2019, 190: 224-246.*

https://doi.org/10.1016/j.earscirev.2018.12.015

摘要：台湾西部沉积物的物源问题是近年来研究争论的焦点。以往研究仅基于碎屑颗粒的 U-Pb 锆石年代学，均认为华南地块水系对台湾的物源具有重要作用，只是贡献量的多少有不同。远源的长江水系（扬子地块）和邻近的珠江、闽江、九龙江等水系（华夏地块）对台湾物源的供给影响一直是研究的主要问题。然而，关于其物源是否真的是华南地块这一根本问题从未被评估过。本文报道了台湾海峡两岸 7 个沉积物样品的锆石 U-Pb 年龄和独居石电子探针（EMP）年龄数据，并综合台湾西部所有河流和沉积地层的已发表数据，以解决这一问题。华南地块所有水系河口沉积物中~1.8 Ga 独居石的缺失或不足，使其不可能成为台湾西部中新世沉积物的来源，该地区~1.8 Ga 独居石颗粒占总年龄谱的 14.5～33.3%。结合中国东南沿海地区早白垩世至近代的构造演化，我们提出了一个新的解释，即马尼拉海沟附近有一个现今隐伏的微大陆。该微大陆可能与冈瓦纳的古元古代造山带有关，最终在约 130～120 Ma 与华南地块发生碰撞，导致其最东端构造单元——平潭—东山变质带（PDMB）抬升。然后在 100 Ma 之后的某个时候分离，分成两部分，其中一部分变成了今天的菲律宾巴拉望-民都洛地区。台湾南部附近的地球物理资料表明，由于南海在 33 Ma 的打开，这个分裂的微大陆的剩余部分沿马尼拉海沟俯冲到菲律宾海板块之下。台湾西部近海的北康和观音基底高地是该微大陆未俯冲的残余，也是台湾西部晚渐新世-中新世沉积的主要物源区。台湾中部雪山山脉始新世-早渐新世地层显示出与始新世-早渐新世及珠江水系近期沉积物相似的锆石和独居石年龄模式，表明台湾原岩的西南起源。这一现象

也符合最近的提出的一种模式，即中央山脉的一部分属于中新世俯冲系统的深部增生楔。

ABSTRACT: The provenance of sediments in western Taiwan has been the subject of debate in recent years. Previous investigators, solely based on the U-Pb zircon geochronology for the detrital grains, all advocated the important roles, but with varying emphasis, of drainage systems in the South China Block. Influence of the Changjiang (Yangtze) River from the far-source Yangtze block versus nearby systems like Zhujiang, Minjiang and Jiulongjiang Rivers in the Cathaysia block has been the main issue. However, the fundamental question of whether the provenance is really the South China Block has never been evaluated. Here we report both the U-Pb zircon and Electron MicroProbe (EMP) monazite age data for seven sediment samples from two sides of the Taiwan Strait and synthesize the published data for all these rivers and sedimentary strata in western Taiwan to tackle this problem. The lack of, or insufficient, ~1.8 Ga monazites in the sediments of river mouths for all drainage systems in the South China Block makes them unlikely to be the source of Miocene sediments in western Taiwan where ~1.8 Ga monazite grains occupy 14.5–33.3% of the total age population. With reference to the tectonic evolution of the coastal southeast China-Taiwan region during Early Cretaceous to recent time, we propose a new explanation that invokes a now-concealed microcontinent along the Manila Trench. This microcontinent, probably related to a Paleoproterozoic orogen in Gondwana, eventually collided with the South China Block causing uplift of the easternmost structural element—the Pingtan-Dongshan Metamorphic Belt (PDMB) at ca. 130–120 Ma. It then drifted away sometime after 100 Ma and split into two parts with one becoming today's Palawan-Mindoro terrain of the Philippines. As indicated by the geophysical data near southern Taiwan, the remainder of this split microcontinent had subducted underneath the Philippine Sea plate along Manila Trench as a result of the opening of the South China Sea at ~33 Ma. Both the Peikang and Kuanyin basement highs in the offshore western Taiwan represent the unsubducted remnants of this microcontinent and also the major suppliers of Late Oligocene-Miocene sediments in western Taiwan. On the other

hand, the Eocene-Early Oligocene strata of the Hsuehshan Range in central Taiwan show both zircon and monazite age patterns resembling the Eocene-Early Oligocene and recent sediments of the Zhujiang drainage system, indicating the southwestern origin of the protolith Taiwan. This scenario also matches the recent proposition that part of the Central Range belongs to the deep-level accretionary prism of a Miocene subduction system.

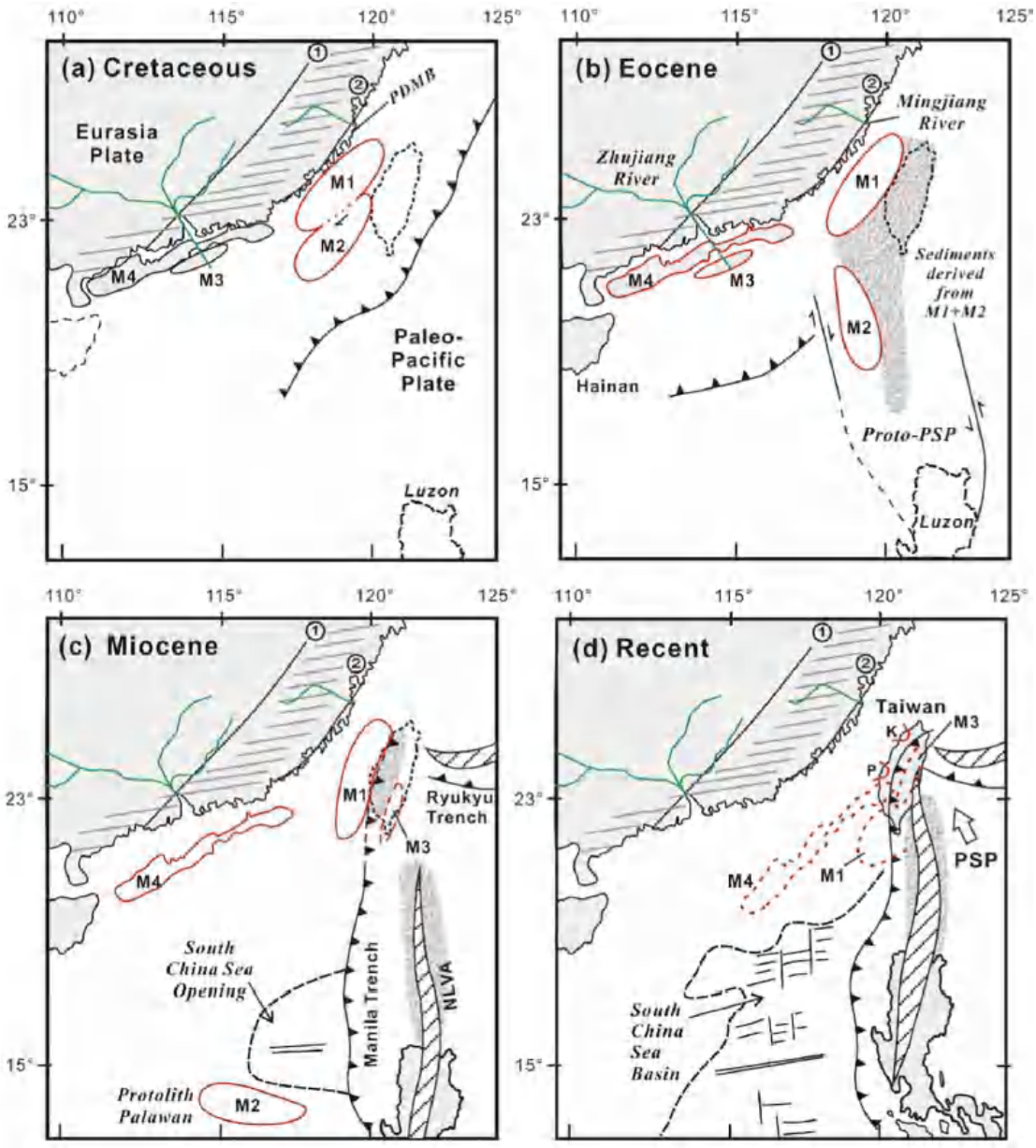

Figure 1. Schematic diagrams showing Cretaceous to recent tectonic evolution as deducted from the provenance study of sediments in western Taiwan. (a) An unknown microcontinent (M1+M2) collided with the coastal southeast China causing the uplift of both the PDMB and the

microcontinent itself. (b) M2 and some continental fragments in the coastal southeast China (M3 and M4) drifted away. Southward movement of M2 was aided by the inception of the proto-Philippine Sea Plate at Eocene (Lallemand, 2016). (c) Opening of South China Sea led to the formation of a subduction system along the Manila Trench and the North Luzon Volcanic Arc (NLVA), and acceleration of M2 to the south and M3 to the north. Part of M1 subducted underneath M3 along the northern extension (now the deformation front) of the Manila Trench. (d) Kuanyin and Peikang Highs (K and P) are the unsubducted remnants of M1. Starting at the Late Miocene (~6 Ma), the arc (NLVA) and continent (M1+M3) collided in the eastern Taiwan. M1: the concealed microcontinent; M2: originally in connection with M1 and now the Palawan-Mindoro of the central Philippines; M3: the protolith Taiwan; M4: the high-magnetic anomaly belt (Cheng, 2004). 1. Lishui-Haifeng fault; 2. Changle-Nanao fault.

9. 石笋年纹层的性质—全球综合

翻译人：杨会会 11849590@mail.sustech.edu.cn

Baker A, Mariethoz G, Comas-bru L, et al. ***The Properties of Annually Laminated Stalagmites-A Global Synthesis****[J]. Reviews of Geophysics,2021,59, e2020RG000722.*

https://doi.org/10.1029/2020RG000722

摘要：年纹层石笋具有提供高频气候变化信息的潜力，且具有良好的年代限制。然而，石笋年纹层具有不同的物理和化学类型，他们形成的共同机制还未被发现。在这里，我们分析了来自 6 个大陆 23 个洞穴的石笋年纹层，试图发现他们形成是否存在共同的机制。年纹层石笋在干旱和半干旱气候区最不常见，在季节性降雨地区最为常见。在全球尺度上，我们观察到纬度越低，年平均温度越高，石笋的生长速率越快。平均增长率的变化点是不常见的，年龄-深度关系表明增长率可以近似为常数。总的来说，年层状石笋具有足够大且混合良好的水源，方解石（石笋）沉淀具有百年尺度上的稳定性，且由于储水与年补给水混合而呈现一阶回归的时间序列谱，以及石笋生长加速的年际频闪（inter-annual flickering），使增长率回到长期均值。当一个多年的气候信号足够强大，足以成为方解石（石笋）生长速率变化的主要控制要素，那么石笋生长速率变化的气候驱动就可以被观察到，这样即使与存储水混合之后产生平滑效应，它（石笋）仍然可以保留了这个气候信号。相比之下，层状石笋的长期稳定生长速度，为进一步提高其无与伦比的年代准确性提供了保障。

ABSTRACT: Annually laminated speleothems have the potential to provide information on high frequency climate variability and, simultaneously, provide good chronological constraints. However, there are distinct types of speleothem annual laminae, from physical to chemical, and a common mechanism that links their formation has yet to be found. Here, we analyzed annually laminated stalagmites from 23 caves and 6 continents with the aim to find if there are common mechanisms underlying their development. Annually laminated stalagmites are least common in arid

and semiarid climates, and most common in regions with a seasonality of precipitation. At a global scale, we observe faster growth rates with increasing mean annual temperature and decreasing latitude. Changepoints in average growth rates are infrequent and age-depth relationships demonstrate that growth rates can be approximated to be constant. In general, annually laminated stalagmites are characterized by centennial-scale stability in calcite precipitation due to a sufficiently large and well-mixed water source, a time series spectrum showing first-order autoregression due to mixing of stored water and annual recharged water, and an inter-annual flickering of growth acceleration, bringing growth rates back to the long-term mean. Climate forcing of growth rate variations is observed where a multi-year climate signal is strong enough to be the dominant control on calcite growth rate variability, such that it retains a climate imprint after smoothing of this signal by mixing of stored water. In contrast, long-term constant growth rate of laminated stalagmites adds further robustness to their unparalleled capacity to improve accuracy of chronology building.

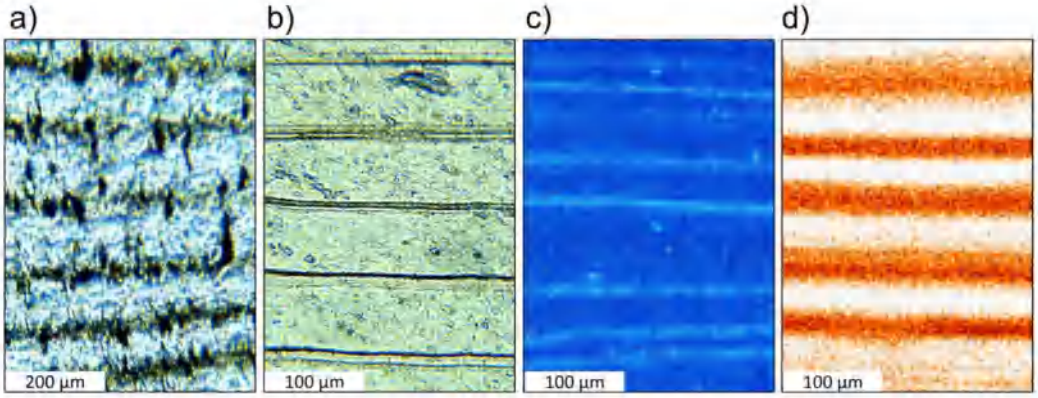

Figure 1. Laminae types. (a) Thin section of calcite fabric/porosity laminae. (b) Thin section of particulate—colloidal organic matter (optically visible); each hydrological year is marked by a 1–4 µm-thick brown lamina often accompanied by a variable number of thinner sub-annual laminae. (c) Thin section of fluorescent organic matter laminae under UV excitation. (d) Chemical laminae (strontium) as mapped by synchrotron radiation—µXRF. Lamina types are not exclusive: fabric laminae can also have chemical cycles and can exhibit fluorescence; particulate—colloidal organic matter laminae are also fluorescent and exhibit chemical cycles, while fluorescent laminae usually exhibit chemical cycles.

Figure 2. Map showing locations of laminated stalagmites investigated here. Gray shaded areas are the global karst extent (Goldscheider et al., 2020).

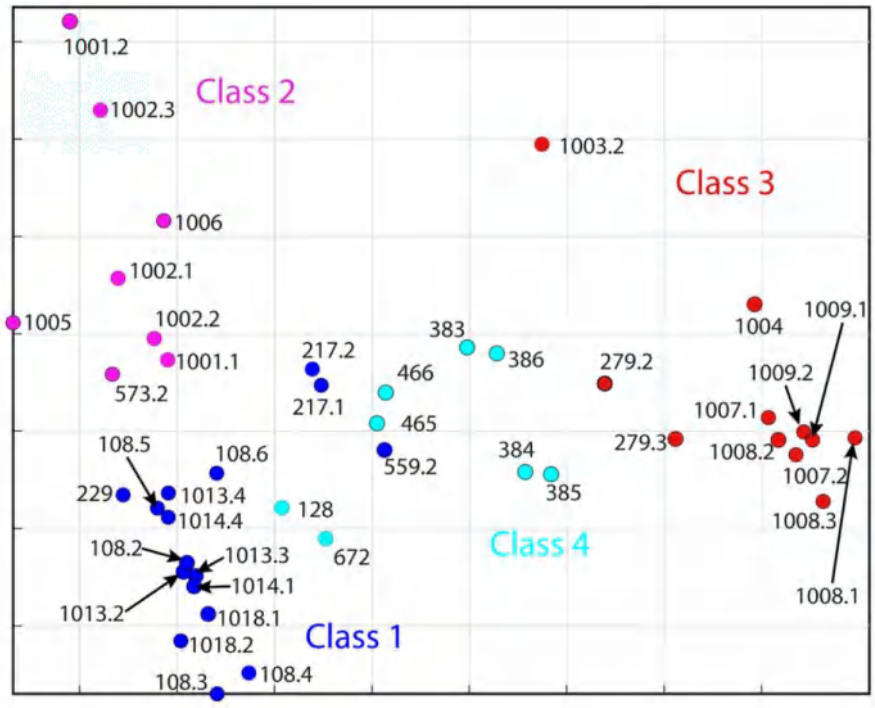

Figure 3. Multidimensional scaling with four clusters. Data included: growth rate; variogram properties range, sill, nugget, and information content (IC); flickering; mean annual temperature; total annual precipitation; potential evapotranspiration; Aridity Index, Precipitation Seasonality Index; modeled recharge, modeled soil and epikarst store percentage fullness, and the Recharge Seasonality Index. The distance chosen is the standardized Euclidean distance. The four clusters are coded by color and samples labeled by entity ID and growth phase (where relevant).

10. 印度尼西亚 Towuti 湖 100 米岩芯的铁矿物学和沉积物颜色反映了集水和成岩条件

翻译人：曹伟 11930854@qq.com

Noriko T, Hiroshi I, Masaru N, et al. ***Iron Mineralogy and Sediment Color in a 100 m Drill Core from Lake Towuti, Indonesia Reflect Catchment and Diagenetic Conditions****[J]. Journal of Volcanology and Geothermal Research, 2021, 22(8): e2020GC009582.*

https://doi.org/10.1029/2020GC009582

摘要：铁是地球表面最丰富的氧化还原敏感元素，沉积体系中富铁相的氧化状态、矿物载体和结晶度可以记录水—岩相互作用和环境条件的细节。然而，我们对这些富铁物质是如何在沉积环境中产生、维持、氧化或还原缺乏全面的了解，尤其是那些具有镁铁质来源的沉积环境。众所周知，印度尼西亚 Towuti 湖的集水区含有丰富的结晶氧化铁，该湖具有悠久的沉积历史。在这里，我们研究了湖中约 100m 长的钻孔岩芯，以了解沉积模式以及地质时期成岩作用对年轻富铁沉积物的影响。我们使用可见/近红外和穆斯堡尔光谱、X 射线衍射、化学测量和统计聚类分析来表征岩芯沉积物。我们发现，岩芯沉积物可分为三个具有统计学差异的区域，分别以镁蛇纹石、铝质粘土矿物和 Fe^{2+}碳酸盐为主。整个岩芯富含纳米相铁，这些区域之间的元素相关性和铁矿物学各不相同。纳米相铁的亚铁和三价铁成分都是高度复杂的，有助于但不决定沉积物颜色的变化。我们认为，这些独特区域是构造盆地变化（尤其是河流夺袭和水系变化）和活性铁深埋引起的成岩叠加的结果。这一复杂记录对解开其他镁铁质湖泊体系的沉积和成岩趋势具有重要意义。

ABSTRACT: Iron is the most abundant redox-sensitive element on the Earth's surface, and the oxidation state, mineral host, and crystallinity of Fe-rich phases in sedimentary systems can record details of water-rock interactions and environmental conditions. However, we lack a complete understanding of how these Fe-rich materials are created, maintained, and oxidized or reduced in sedimentary environments, particularly those

with mafic sources. The catchment of Lake Towuti, Indonesia, is known to contain a wide range of abundant crystalline Fe oxide, and the lake has a long sedimentary history. Here, we study a ~100 m long drill core from the lake to understand patterns of sedimentation and how young iron-rich sediments are affected by diagenesis through geologic time. We use visible/near infrared and Mössbauer spectroscopy, X-ray diffraction, bulk chemistry measurements, and statistical cluster analysis to characterize the core sediment. We find that the core sediment can be divided into three statistically different zones dominated by Mg serpentine, Al clay minerals, and Fe^{2+} carbonate, respectively. The entire core is rich in nanophase Fe, and elemental correlations and Fe mineralogy vary between these zones. The nanophase Fe is highly complex with both ferrous and ferric components, and contributes to, but does not dictate, variations in sediment color. We propose that the distinctive zones are the result of structural basin changes (notably river capture and shifting drainage patterns), and diagenetic overprinting caused by deep burial of reactive Fe. This complex record has implications for disentangling depositional and diagenetic trends in other mafic lacustrine systems.

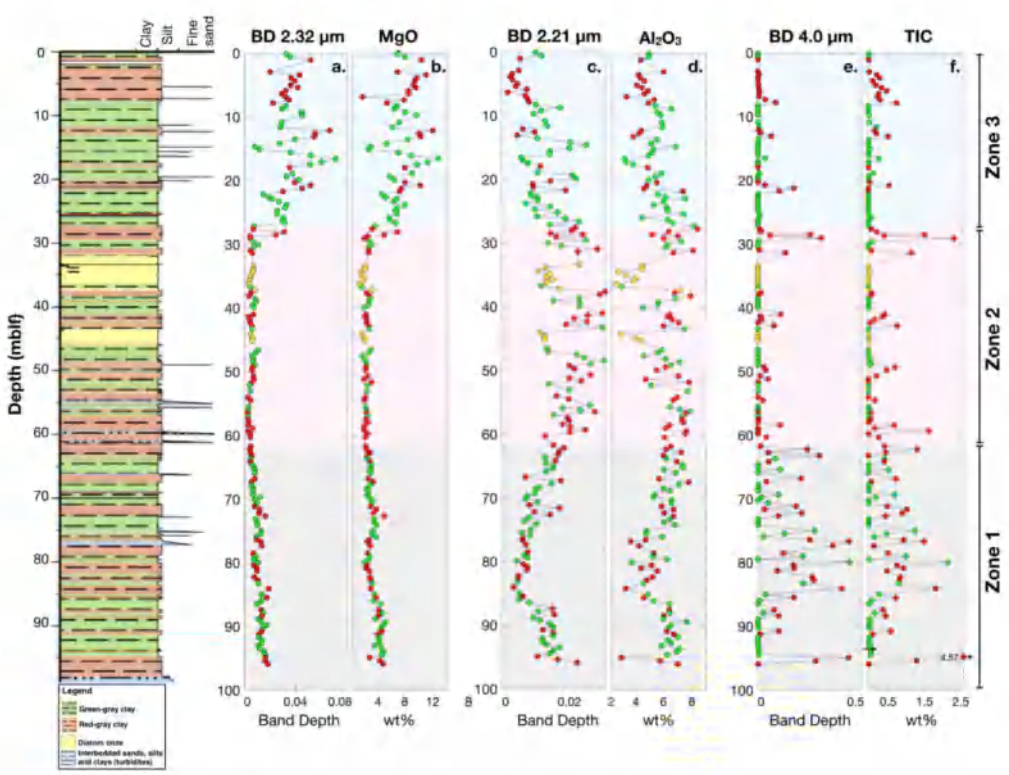

Figure 1. Down-core plots of each core sample's (a) Mg-OH absorption band depth, (b) MgO elemental abundance, (c) Al-OH absorption band depth, (d) Al_2O_3 elemental abundance, (e) CO_3 absorption band depth, and (f) total inorganic carbon. The color of each dot represents the qualitative color of the wet core, determined at LacCore immediately after splitting the core section, with yellow representing pure diatomaceous ooze. Each Zone identified using breakpoint analysis is a different color (Zone 3 blue, Zone 2 pink, Zone 1 gray).

11. 气候交替驱动土壤磁性颗粒形成过程中的协同和竞争关系

翻译人：李海 12031330@mail.sustech.edu.cn

Cai Y, Long X, Meng X, et al. ***Coordinated and competitive formation of soil magnetic particles driven by contrary climate development****[J]. Geophysical Research Letters, 2021, 48, e2021GL094506.*

https://doi.org/10.1029/2021GL094506

摘要：亚铁磁性（FM）和反铁磁性（AFM）的氧化铁颗粒被认为是土壤成因和气候指标，因为它们随着降雨和温度的增加而富集。然而，降雨和温度的相反变化导致相对湿度（RH）的快速变化，这可能导致它们的竞争和转化。作者研究了青藏高原东缘经历了相反气候发展的两个土壤序列。低相对湿度的干燥温暖气候有利于 AFM 赤铁矿和 FM 颗粒的协同富集，而高相对湿度的潮湿凉爽气候主要产生针铁矿，但导致低含量 AFM 赤铁矿和 FM 颗粒之间的竞争。结果很好地解释了土壤和沉积物中颜色和磁性之间的变化关系，并表明在基于氧化铁的古气候重建中，温度与降水一样重要，尤其是在强干湿循环和气候模式变化期间。

ABSTRACT: Ferrimagnetic (FM) and antiferromagnetic (AFM) iron oxide particles are considered pedogenic and climatic indicators due to their enrichment with comparable increasing in rainfall and temperature. However, the opposite changes in rainfall and temperature result in rapid change of relative humidity (RH), which could lead to their competition and transformation. We examined two soil sequences which have undergone contrary climate development on the eastern edge of the Tibetan Plateau. Dry and warm climate with low RH favors the coordinative enrichment of AFM hematite and FM particles, while wet and cool climate with high RH mainly produces goethite but leads to competition between low content AFM hematite and FM particles. The outcome well interprets the changing relationship between color and magnetism in soils and sediments, and suggests that temperature is as important as precipitation in paleoclimate reconstruction based on iron oxides, especially during

strong dry-wet cycles and climate pattern shifts.

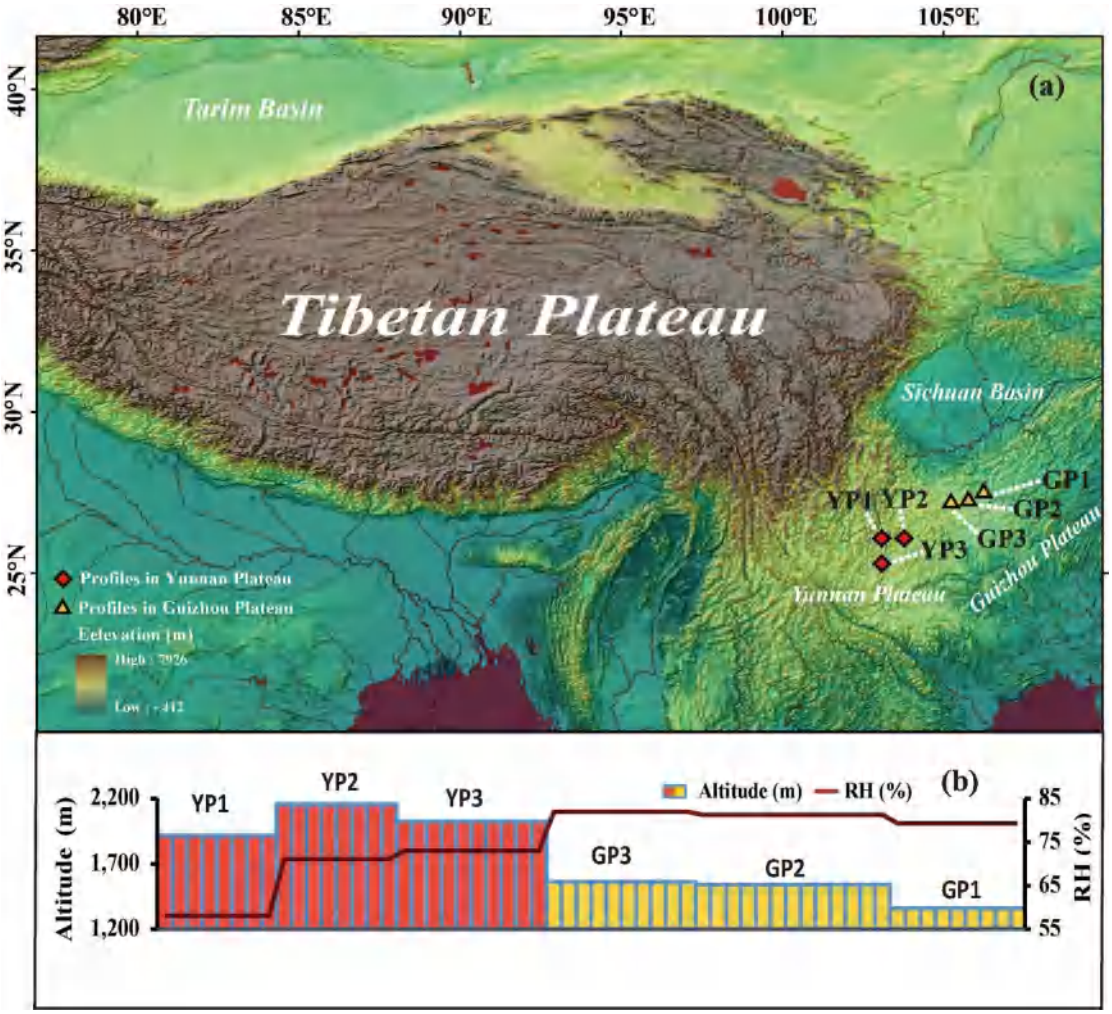

Figure 1. (a) Sampling locations in the Yunnan Plateau (YP) and Guizhou Plateau (GP) on the east edge of the Tibetan Plateau (TP); (b) The YP is characterized by higher altitude and lower relative humidity (RH) than the GP. The profiles of YP1, YP2, YP3 and GP1, GP2, GP3 with increasing relative humidity were sampled in the YP and GP, respectively.

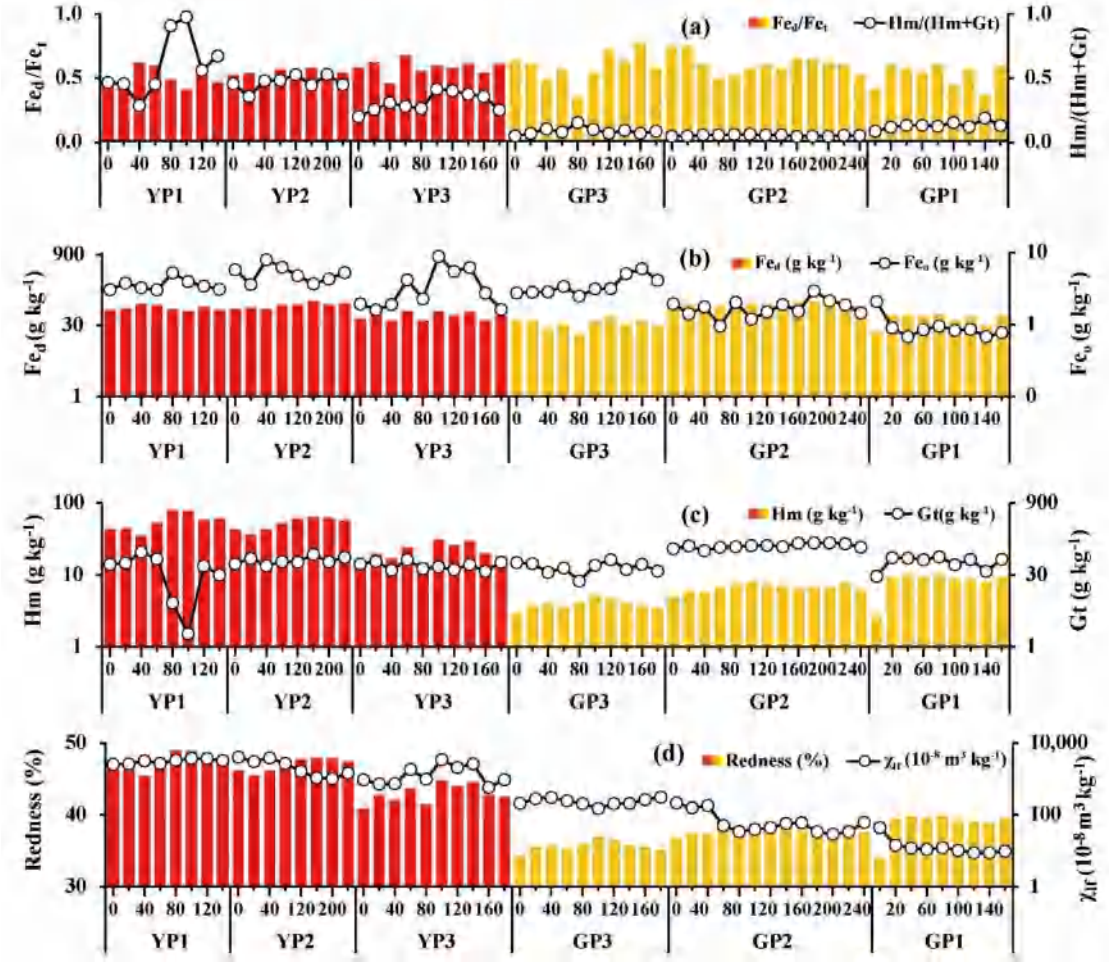

Figure 2. Fe_d/Fe_t is comparable in both sequences but Hm/(Hm+Gt) which is controlled by RH, is much higher in the YP sequence than that in the GP sequence (a). The ranges of Fe_d and Fe_o are also similar in both sequences (b) while Hm is significantly higher in the YP sequence and Gt is slightly higher in the GP sequence (c). The magnetic susceptibility (χ_{lf}) changes in phase with the redness in the YP sequence but out of phase in the GP sequence (d). Note that the range of the date is large, in order to facilitate comparison, the coordinates of partial parameters in the figure are expressed by logarithms.

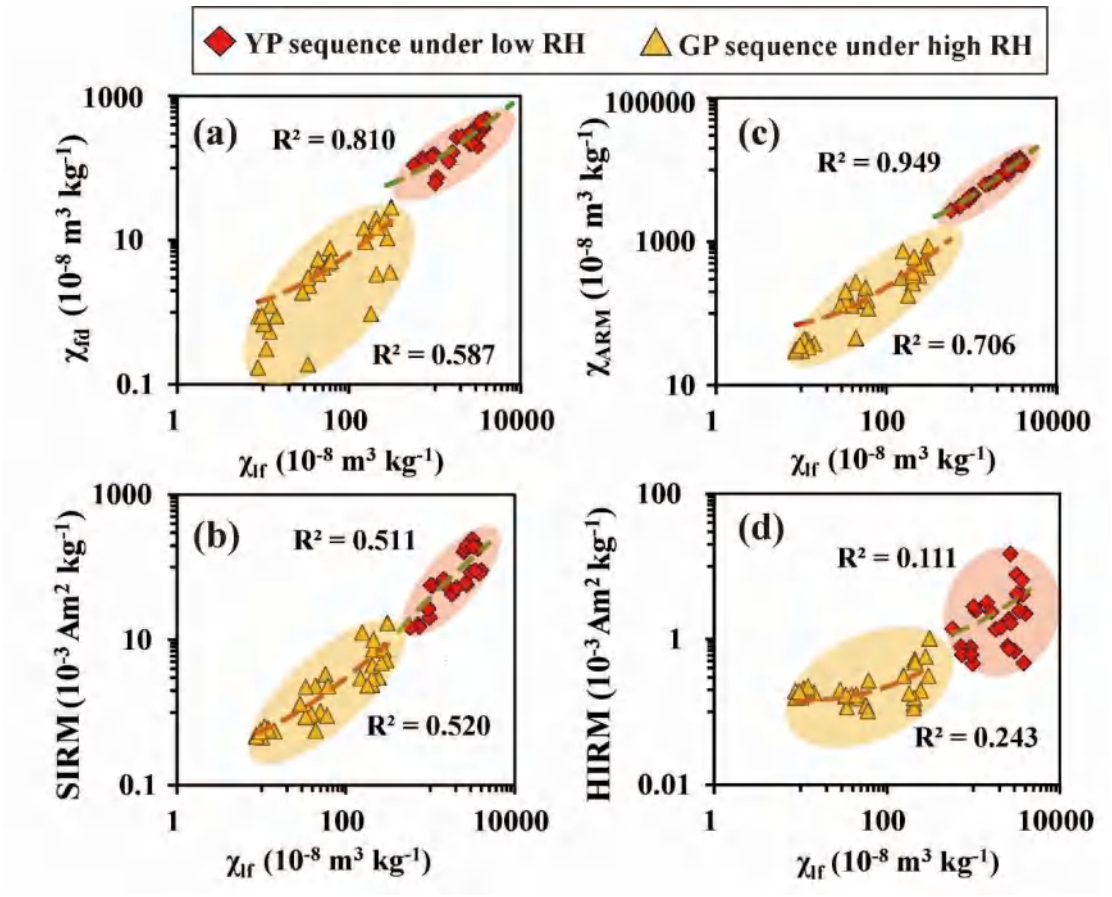

Figure 3. The magnetic parameters χ_{fd}, χ_{ARM}, SIRM are commonly higher in the YP sequence than the GP sequence and change consistently with the increase of χ_{lf} in both sequences (a-c) except for the HIRM (d). Note that the range of the date is large, in order to facilitate comparison, the coordinates in the figure are expressed by logarithms.

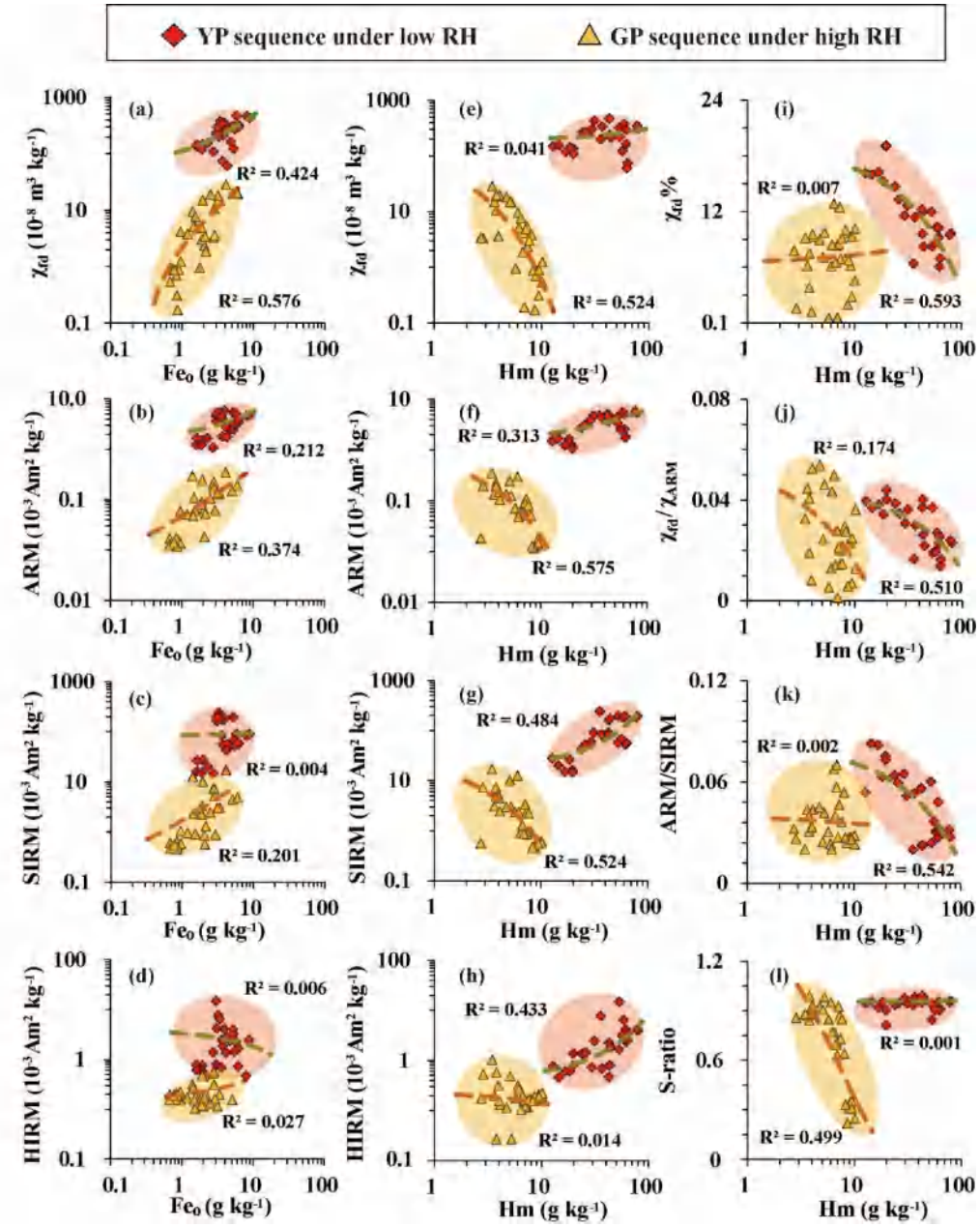

Figure 4. The magnetic parameters χ_{fd}, ARM, SIRM generally increase with Fe_o (a-c) except for HIRM (d). Both, the FM particles and Hm, are more enriched and change in phase in the YP sequence, while they are less enriched and change out of phase in the GP sequence (e-g) except that HIRM demonstrates more consistent correlation with Hm in both sequences (h). In the YP sequence, the magnetic parameters χ_{fd}%, χ_{fd}/χ_{ARM}, ARM/SIRM decrease significantly with Hm (i-k) but the S-ratio keeps close to 1 (l). In the GP sequence, however, these ratio parameters exhibit no significant trend with Hm (i-k) but the S-ratio demonstrates significant decrease with Hm (l). Note that the range of the date is large, in order to facilitate comparison, the coordinates in the figure are expressed by logarithms.

12. 冰下和近海沉积重建的 Larsen C 冰架演化历史

翻译人：张亚南 zhangyn3@mail.sustech.edu.cn

Smith J. A, Hillenbrand C. D, Subt C, et al. ***History of the Larsen C Ice Shelf reconstructed from sub–ice shelf and offshore sediments****[J]. Geology, 2021,49(8), 978-982.*

https://doi.org/10.1130/G48503.1

摘要：由于冰架对气候强迫的响应具有多种时间尺度，范围从年际变化到千年尺度。因此，对冰架长期历史的了解有利于预测其未来的演化。作者通过冰架下方和近海沉积物岩心数据，首次详细重建了南极半岛东部 Larsen C 冰架（LCIS）。沉积学和年代学结果显示，扩张的南极半岛冰盖接地线（grounding line, GL）在 17.7 ± 0.53 之前就开始从大陆架中部后撤，在~ 6 k.y 后冰崩线（Calving line, CL）也后撤到大陆架中部。早在 9.83 ± 0.85 kyr GL 已经到达内陆架。自 7.3 ka 以后，冰盖经历了 2 期后撤但并没有崩解，表明全新世冰盖稳定性的气候界限并未被打破。未来 LCIS 的崩塌将证实南极半岛东部的冰盖消减和潜在的气候强迫的程度，在过去 11.5 k.y 都是前所未有的。

ABSTRACT: Because ice shelves respond to climatic forcing over a range of time scales, from years to millennia, an understanding of their long-term history is critically needed for predicting their future evolution. We present the first detailed reconstruction of the Larsen C Ice Shelf (LCIS), eastern Antarctic Peninsula (AP), based on data from sediment cores recovered from below and in front of the ice shelf. Sedimentologic and chronologic information reveals that the grounding line (GL) of an expanded AP ice sheet had started its retreat from the midshelf prior to 17.7 ± 0.53 calibrated (cal.) kyr B.P., with the calving line following ~6 k.y. later. The GL had reached the inner shelf as early as 9.83 ± 0.85 cal. kyr B.P. Since ca. 7.3 ka, the ice shelf has undergone two phases of retreat but without collapse, indicating that the climatic limit of LCIS stability was not breached during the Holocene. Future collapse of the LCIS would therefore confirm that the magnitudes of both ice loss along the eastern AP and underlying

climatic forcing are unprecedented during the past 11.5 k.y.

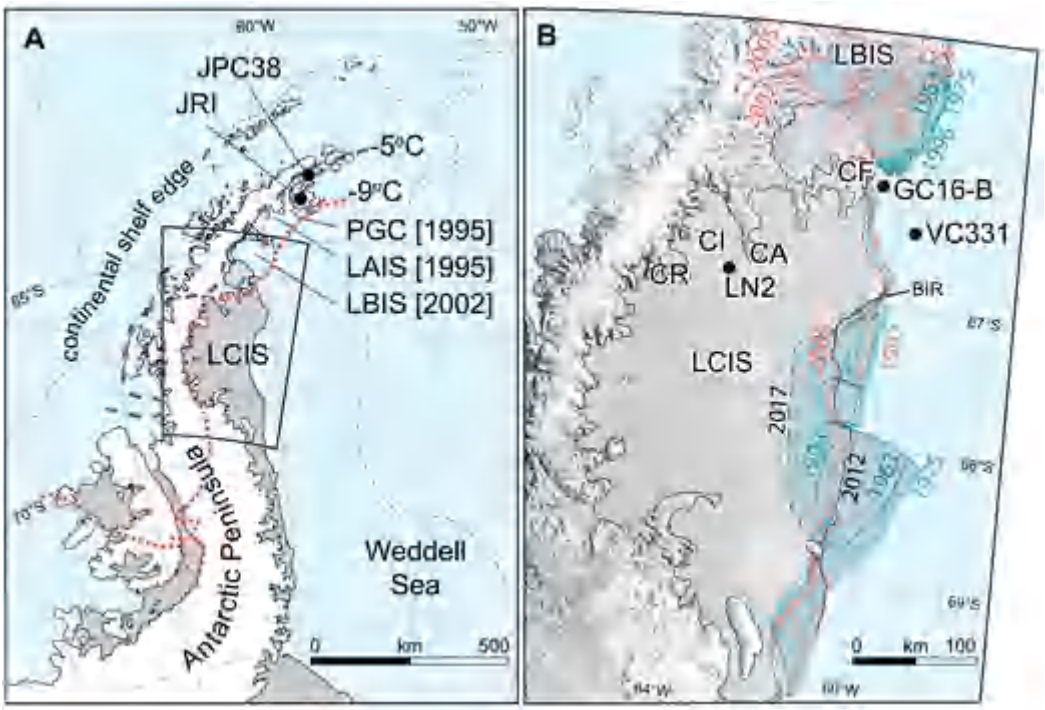

Figure 1. (A) Map of the Antarctic Peninsula (AP) showing Prince Gustav Channel (PGC), Larsen A (LAIS), Larsen B (LBIS), and Larsen C (LCIS) ice shelves, James Ross Island (JRI) ice core, and sediment core JPC38. Year of contemporary collapse is given in brackets. Red dotted and blue dashed line refer to −9 °C and −5 °C isotherms, respectively (Morris and Vaughan, 2003). (B) Map of LCIS showing cores LN2, VC331, and GC16-B, and Cabinet Inlet (CI), Cape Roberts (CR), Cape Alexander (CA), Cape Framnes (CF), and Bawden ice rise (BIR). Colored lines show historical calving line positions.

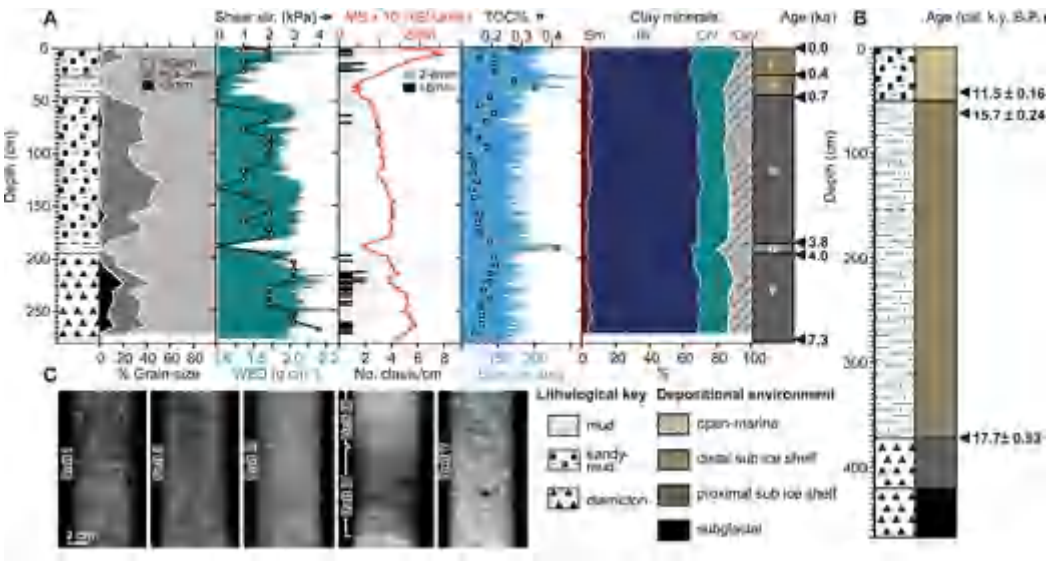

Figure 2. (A) Core data for LN2 (Larsen C Ice Shelf, 66°52.0′S, 62°54.0′W). Relative paleointensity (RPI) ages (ka) are given alongside five lithological units/depositional environments. WBD—wet-bulk density, MS—magnetic susceptibility, TOC—total organic carbon, Sm—smectite, Illi—illite, Chl—chlorite, Kaol—kaolinite. (B) Core lithology (adapted from Curry and Pudsey, 2007) and ramped pyrolysis (PyrOx) ^{14}C ages (cal. kyr B.P.) for core VC331 (66°26.1′S, 59°57.6′W). (C) X-radiographs of lithological units (I – V) in core LN2.

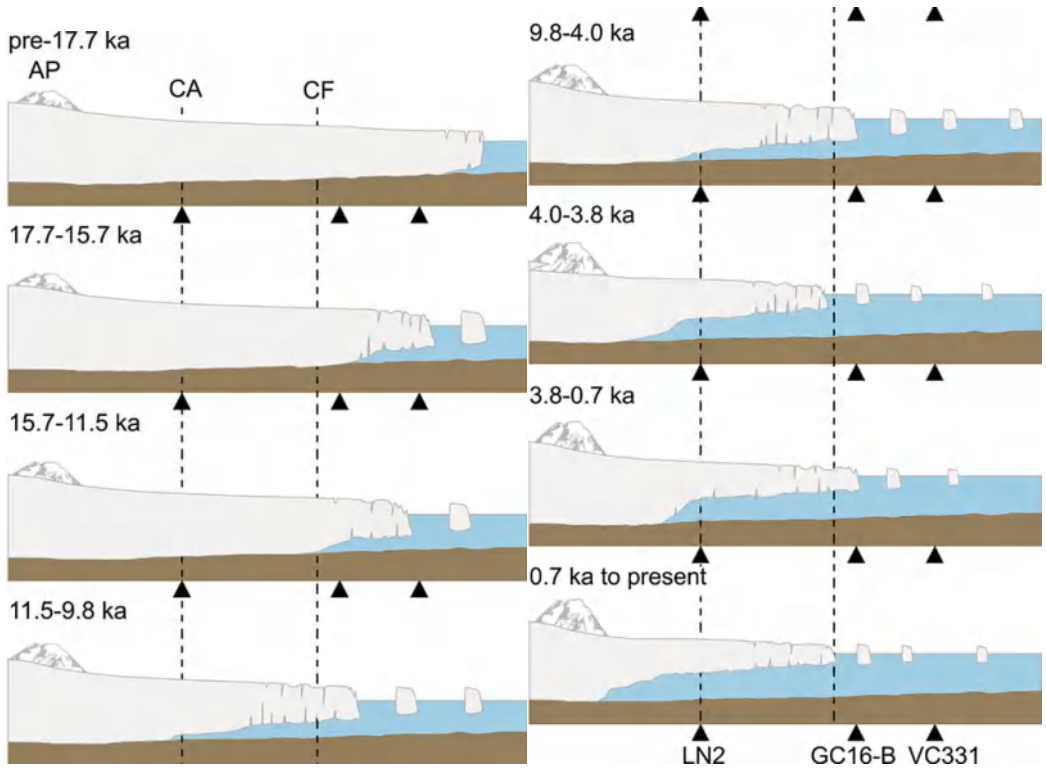

Figure 3. Reconstruction of the Larsen C Ice Shelf (LCIS) ca. 17.7 ka to present. Vertical lines

denote relative positions of Cape Alexander (CA) and Cape Framnes (CF). Antarctic Peninsula (AP) is also shown. Ages for core GC16-B are from Subt et al. (2017), and ice-sheet thinning is inferred from Jeong et al. (2018).

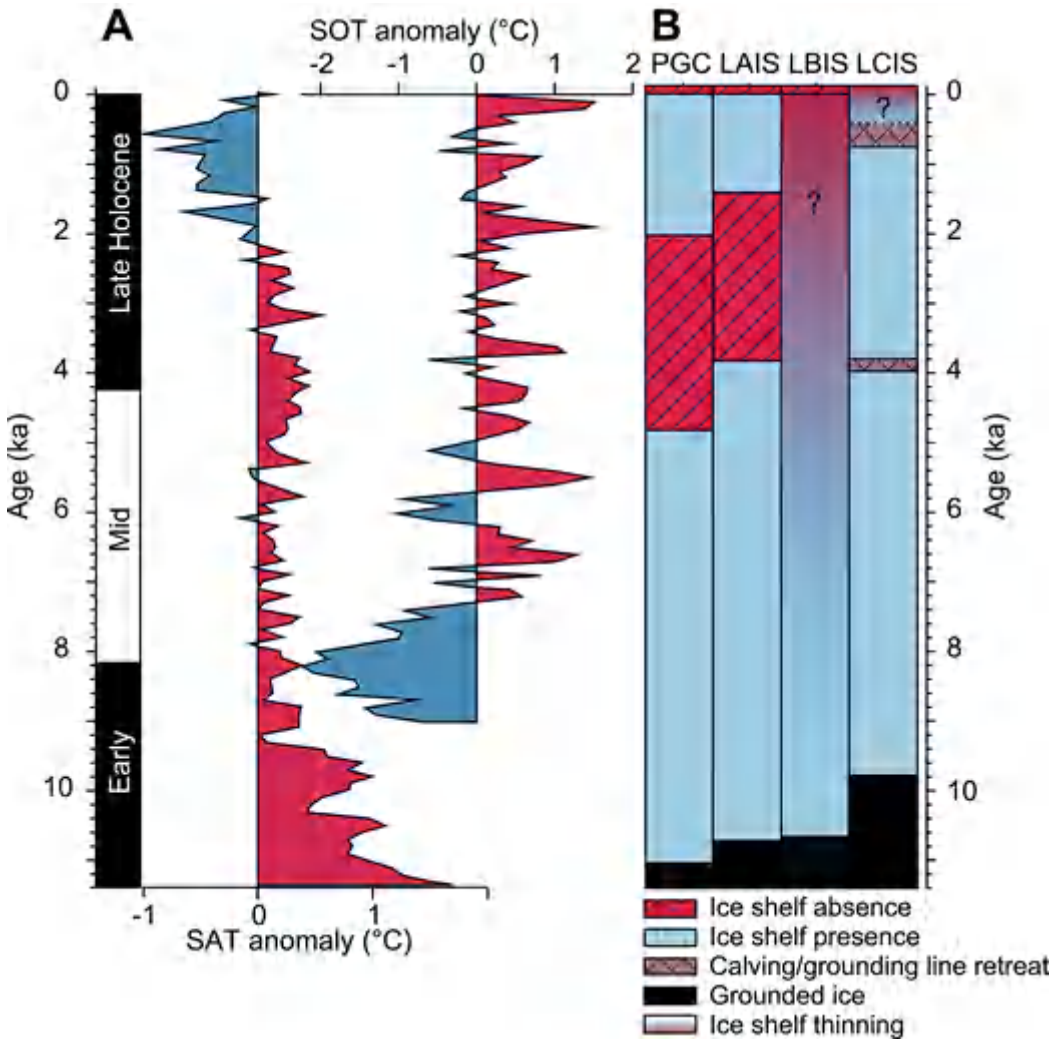

Figure 4. (A) Reconstructed surface air temperature (SAT) (Mulvaney et al., 2012) and surface ocean temperature (SOT) (Etourneau et al., 2019), plotted as positive/negative anomalies from 0 °C. (B) Holocene history of Prince Gustav Channel (PGC) (Pudsey and Evans, 2001), Larsen A Ice Shelf (LAIS) (Brachfeld et al., 2003), Larsen B Ice Shelf (LBIS) (Domack et al., 2005; Jeong et al., 2018), and Larsen C Ice Shelf (LCIS) (this study). Onset of thinning of LBIS (Domack et al., 2005) and late Holocene thinning and retreat of LCIS are uncertain.